

# Assessing raindrop evolution over northern Western Ghat from stable isotope signature of rain and vapour

Sheena Sunil Nimya<sup>1,2</sup>, Sundara Pandian Rajaveni<sup>1</sup>, Saikat Sengupta<sup>1\*</sup>, Sourendra Kumar Bhattacharya<sup>3</sup>, Nandhini Ananthvel<sup>1</sup>

<sup>1</sup>Center for Climate Change Research, Indian Institute of Tropical Meteorology, Ministry of Earth Sciences, Pune-411008, India

<sup>2</sup>Department of Earth, Atmospheric and Planetary Sciences, Purdue University, West Lafayette, IN, USA

<sup>3</sup>Institute of Earth Sciences, Academia Sinica, Taipei 11529, Taiwan

\*Correspondence: Saikat Sengupta (saikat@tropmet.res.in)

## Abstract

Stable isotopes of hydrogen and oxygen were analyzed in rain and vapour samples collected simultaneously from Pune, India, during the 2019 summer monsoon. The  $\delta^{18}\text{O}$  and  $\delta\text{D}$  were significantly depleted in four events when the Outgoing Longwave Radiation showed a strong negative anomaly, suggestive of large-scale convection. The  $\delta^{18}\text{O}$  values of the rain samples are negatively correlated with their d-excess, indicative of modification of raindrops by evaporation. Analysis of the isotope data indicates isotope exchange between rain and ambient vapour and associated raindrop evaporation in the sub-cloud layer. Using the  $\Delta\delta$ - $\Delta\text{d}$  diagram method of assessing sub-cloud rain and vapour exchange, our data suggest an equal share of equilibrium exchange and drop evaporation.

We used a one-dimensional Below Cloud Interaction Model to quantify sub-cloud processes affecting raindrop evolution. A Rayleigh ascent assumption in BCIM simulations yields higher rain isotope values, although model and observed values are well correlated. Using radiosonde-based temperature and humidity profiles and constructing vapour isotope profiles from a combination of satellite (Tropospheric Emission Spectrometer) data and a global circulation model (LMDZ) output, simulations improve the agreement of the model with observed values. Sensitivity studies reveal that model values are strongly influenced by vapour isotope ratios, and moderately by drop size, temperature and relative humidity. Raindrop evaporation estimated from mass change in the model shows that, on a daily scale, the drop evaporation varies from 4% to 61% and, on average, 23% of the drop mass evaporated in this region. It is seen that the raindrop evaporation reduces the rainfall, especially in the lower range of precipitation. The evaporation also influences the heat budget, affecting monsoon convection.

## 42 1. Introduction

43 The Intergovernmental Panel on Climate Change (IPCC) has emphasized the importance of recycled  
44 moisture in the atmosphere (IPCC, 2014). Moisture recycling includes processes by which a fraction of the  
45 precipitated water returns to the atmosphere and causes further precipitation over the same area (Gray, 2012).  
46 These processes are soil evaporation, transpiration from plants, intercepted or condensed water on leaves, and  
47 evaporation from falling raindrops (Brubaker et al., 1993; Trenberth, 1999). This recycling increases with  
48 ambient temperature but decreases with humidity (Pranindita et al., 2022; Zaitchik et al., 2006; Zhang et al.,  
49 2021). It has been seen (Kumar et al., 2021; Pathak et al., 2014) that a high precipitation recycling ratio (~15%)  
50 pertains over India during the Indian Summer Monsoon (ISM; June-September). Among the contributing  
51 factors, raindrop evaporation is difficult to estimate because the parameters needed for estimating rain  
52 evaporation are not accurately available from satellite sources.

53 Stable isotopologues ( $^1\text{H}_2^{18}\text{O}$ ,  $^1\text{H}^2\text{H}^{16}\text{O}$ ,  $^1\text{H}_2^{16}\text{O}$ ) of rain waters can be used to assess the magnitude of  
54 raindrop evaporation (Crawford et al., 2017; Rahul et al., 2016; Salamalikis et al., 2016; Wang et al., 2021; Xiao  
55 et al., 2021). Falling raindrops exchange isotopes with the ambient vapour; this happens throughout the fall but  
56 occurs mostly in the unsaturated sub-cloud layer. The magnitude of this exchange, which alters the rain isotope  
57 ratios, can be used to quantify the extent of raindrop evaporation. Using satellite-based observations of vapour  
58 isotopologues ( $^1\text{H}^2\text{H}^{16}\text{O}$  and  $^1\text{H}_2^{16}\text{O}$ ) and an isotope mass balance model, Worden et al. (2007) estimated that in  
59 the tropics, nearly 20 % of the mass of raindrops evaporates. However, they noted that the satellite data has  
60 limited temporal and spatial coverage. Therefore, estimating drop evaporation on a daily to monthly scale is  
61 difficult. Raindrop evaporation has also been estimated from ground-based rain isotope observations and a set of  
62 empirical equations (Froehlich et al., 2008; Li et al., 2021; Wang et al., 2016; Zhu et al., 2021). However, it is a  
63 challenge to account for all cloud microphysical processes and their associated isotopic fractionations.  
64 Normally, these processes are considered for simulating rain isotope values in various General Circulation  
65 Models (GCM; Risi et al., 2019; Yoshimura et al., 2008; Stewart, 1975). But recent studies have shown that  
66 most of these GCMs fail to estimate raindrop evaporation correctly in tropical India (Nimya et al., 2022;  
67 Sengupta et al., 2023). This is possibly due to the coarseness of grid sizes used in these GCMs, which are  
68 inadequate to capture the region-specific complexities of processes controlling the evaporation. This necessitates  
69 controlled isotope observations and region-specific models for proper estimation of this parameter (Aemisegger  
70 et al., 2015).

71 Various approaches have been followed to estimate raindrop evaporation using paired observations of  
72 rain and vapour isotopes. For example, a bin resolved microphysical model was used to quantify drop  
73 evaporation during the Atlantic Tradewind Ocean–Atmosphere Mesoscale Interaction Campaign (ATOMIC;  
74 Sarkar et al., 2023). Graf et al. (2019), based on surface rain and vapour isotope observations in Zurich,  
75 Switzerland, developed a simple one-dimensional model (Below Cloud Interaction Model, BCIM) which  
76 considers various cloud microphysical processes during raindrop formation (condensation, vapour deposition,  
77 riming, etc.) as well as evaporative exchange processes within and below the cloud. This model simulates the  
78 isotopic evolution of an ice/liquid drop as it undergoes exchange processes while falling to the ground.  
79 However, being a one-dimensional vertical model, it does not consider any moisture advection and downdraft.

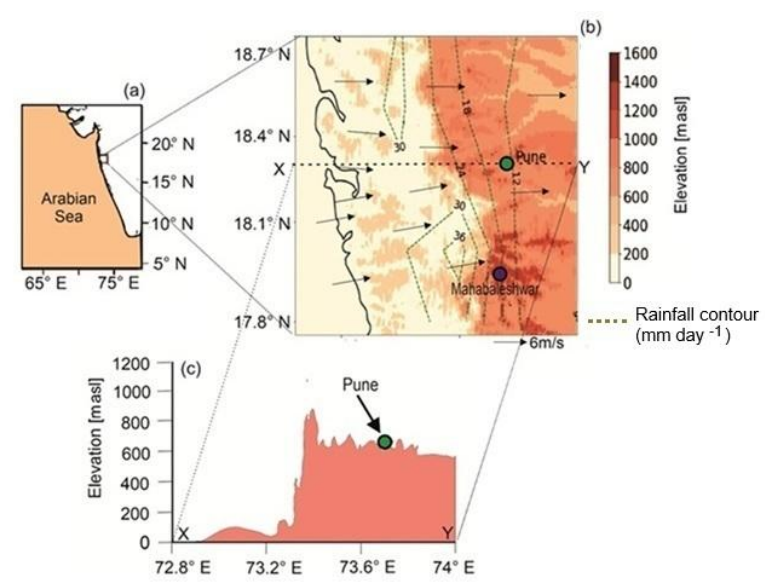
80 In the tropical Western Ghat (WG) region of India, shallow convective clouds are the dominant types  
81 (80 % of clouds occur below 4 km and 45 % below 2.5 km altitude) during the ISM (Konwar et al., 2014).

82 Faster evaporation of smaller raindrops associated with intense rainfalls from these clouds provides significant  
 83 positive energy feedback to form mesoscale convection (Konwar et al., 2014; Tao et al., 2012). A study of drop  
 84 size distributions showed that raindrop evaporation prevails in the warm rain process occurring in this region  
 85 (Murali Krishna et al., 2021). The current study investigates the applicability of the BCIM to predict rain  
 86 isotopes and rain drop evaporation in Pune, situated on the lee side of the WG, using paired observations of rain  
 87 and vapour isotopes during ISM.

88  
 89 **2. Experimental Methodology**

90 **2.1 Study area**

92 Rainwater and vapour samples were collected from the ground level at the Indian Institute of Tropical  
 93 Meteorology (18.53° N, 73.85° E), Pune during the summer monsoon of 2019. This region receives >90 %  
 94 rainfall during the ISM and is situated at the lee side of the Western Ghat mountain (Fig. 1). Rainfall in Western  
 95 India occurs from mid-tropospheric low-pressure systems in several episodes, each of which usually lasts for 2–  
 96 3 days. These systems are locked in place during these periods and fed by moisture derived from the Arabian  
 97 Sea (Wang et al., 2006; Rao, 1976). The geographic location of the region, its altitude, rainfall variation across  
 98 the WG mountains, and the topographic profile across Pune are shown in Fig. 1. There is a sharp variation of  
 99 rainfall across the mountains from the coastal zone (30 mm day<sup>-1</sup>) to the lee side (12 mm day<sup>-1</sup>) which is a  
 100 characteristic of orography-induced rainfall (Fig. 1). The surface air temperature in Pune varies from 20° C to  
 101 30° C during the ISM (Pattanaik et al., 2019).



102  
 103 **Figure 1.** (a) The location of the study area in India. (b) Topographic map of the northern Western Ghat, India (prepared  
 104 based on the GTOPO30 digital elevation model). The rainfall contours (long-term mean June-September rainfall in mm day<sup>-1</sup>)  
 105 were constructed using gridded (0.25°x0.25°) rainfall data (1901-2020) from the India Meteorological Department (IMD).  
 106 (c) A topographic profile along the latitude 18.53° N through Pune (Green circle at an altitude of 560 m) shows its position.

107  
 108 **2.2 Sample Collection, Isotope Measurements**

109 The onset and withdrawal dates of ISM (based on wind direction, specific humidity, and Outgoing  
 110 Longwave Radiation, OLR; IMD, 2019) at Pune in 2019 were 22 June 2019 and 4 October 2019, respectively.

111 Rainwater samples were collected during 2019 monsoon using samplers made following the guidelines of the  
112 International Atomic Energy Agency (see SI-1 and Fig. S1-1). For vapour samples, an in-house fabricated glass  
113 condenser was used (see SI-2 and Fig. S2-1). Twenty-nine vapour samples were collected during the rainy days,  
114 along with rain samples (avoiding direct rain splash entry), and fourteen samples were collected during non-  
115 rainy days. The vapour collection efficiency was estimated from the amount collected against the amount  
116 expected (see Table S2-1). Due to logistical problems, vapour samples could not be collected before mid-July.

117 The samples (rain water and condensed vapour) were measured using a Liquid Water Isotope Analyser  
118 (Model Number TIWA-45-EP, Los Gatos Research). This instrument measures liquid samples using Off-Axis  
119 integrated cavity output spectroscopy (OA-ICOS) with a routine precision of 0.1 ‰ and 1 ‰ for  $\delta^{18}\text{O}$  and  $\delta\text{D}$ ,  
120 respectively, relative to VSMOW (Rajaveni et al., 2024; see also SI-3). The d-excess values defined as: d-excess  
121 =  $\delta\text{D} - 8 \cdot \delta^{18}\text{O}$  (Dansgaard, 2012) have a precision of 1 ‰. The reported rain isotope data are given after being  
122 weighted by the amount of rainfall on that day.

123

### 124 **2.3 Ground-based meteorological, Radiosonde and Satellite data**

125 The rainfall data are obtained from the Pune observatories of the IMD, available at the National Data  
126 Centre ([www.imdpune.gov.in/ndc\\_new/ndc\\_index.html](http://www.imdpune.gov.in/ndc_new/ndc_index.html)). Apart from rainfall, daily average temperature and  
127 relative humidity data from the Pune observatory were also obtained. The daily gridded data (zonal and  
128 meridional wind, specific humidity, air temperature, and cloud liquid water content) from the European Centre  
129 for Medium-Range Weather Forecasts Reanalysis (ERA5) dataset with a resolution of  $0.25^\circ \times 0.25^\circ$  (Hersbach et  
130 al., 2020) and the Interpolated Outgoing Longwave Radiation (OLR) data ( $2.5^\circ \times 2.5^\circ$ ) from NOAA  
131 (<https://psl.noaa.gov/data/gridded/data.olrchr.interp.html>) are used in this study.

132 The upper-air radiosonde measurements (relative humidity (RH); temperature (T)) carried out over  
133 Pune were obtained from the University of Wyoming repository  
134 (<http://weather.uwyo.edu/upperair/sounding.html>). The values at every 50 mb interval (about 470 m in height)  
135 of the two parameters were available for two time periods: starting at 00 UTC and starting at 12 UTC, yielding  
136 two profiles for each day. For our use on the daily scale, the two profiles for each parameter (RH and T) were  
137 averaged to make a representative daily profile. Since the input for BCIM is required at every 1-meter interval, a  
138 linear interpolation between two consecutive pressure levels in logarithmic scale (Ingleby et al., 2016) was  
139 carried out. However, the zone between the cloud base (lifting condensation level, LCL) and the drop  
140 introduction height (taken as the Cloud Liquid Water Content (CLWC) peak) poses a problem. As the BCIM  
141 requires RH=100 % for the formation of water droplets, the RH values above the LCL and up to the CLWC  
142 peak were considered as 100 %, disregarding the radiosonde data above the LCL (see section 2.4.2 and SI-6b).  
143 The typical uncertainty of T and RH is  $0.3^\circ\text{C}$  (Sapucci et al, 2005; Jensen et al., 2016) and 8 % (Xu et al., 2023)  
144 respectively.

145 Tropospheric Emission Spectrometer (TES) Level 2 (Nadir-Lite-Version 6) retrievals of HDO and  $\text{H}_2\text{O}$   
146 data for the available period (2005–2007) are used to construct mean vapour  $\delta\text{D}$  ( $\delta\text{D}_v$ ) profiles (discussed later).  
147 The details of quality control criteria and biases associated with TES observations are discussed by Herman et  
148 al. (2014) and Worden et al. (2011). Grid point observations of  $\delta\text{D}_v$  by TES have a precision of  $\sim 10\text{--}15\text{ ‰}$ ,  
149 which reduces to  $1\text{--}2\text{ ‰}$  when the data are averaged over a larger region (Lee et al., 2011; Pradhan et al., 2019).

150 To decipher the moisture sources for vapour/rain at and around our study area, 48-hour air mass back  
151 trajectory analysis was carried out at 850 mb pressure level using the NOAA Hybrid Single-Particle Lagrangian  
152 Integrated Trajectory (HYSPPLIT) model (Draxler and Hess, 1997). The model tracks the movement of air  
153 parcels backward from a given location for a desired period (see SI-4).

154

## 155 **2.4 The input parameters for BCIM**

156 As mentioned earlier, to quantify the sub-cloud processes altering the rain isotope values, we used the  
157 BCIM (Graf et al., 2019). A brief description of this model, for application to the shallow cloud processes over  
158 Pune, is provided here. The model comprises a single vertical column that extends from the ground level to the  
159 point at which a single hydrometeor is introduced. Within this column, the hydrometeor descends under the  
160 influence of gravity, undergoes growth or evaporation (depending upon the ambient humidity and temperature),  
161 changes its isotopic composition through equilibrium and kinetic isotope exchange with surrounding vapour,  
162 and finally reaches the surface as a raindrop. The final isotopic composition of the drop is estimated following  
163 four steps of calculations: (1) setting up the initial condition involving the drop introduction height and its size,  
164 (2) estimation of the initial isotopic composition of the hydrometeor, (3) tracking the microphysical evolution of  
165 a falling hydrometeor, and (4) tracking the changes in isotopic composition of the hydrometeor along the  
166 descent. For these calculations, the model requires altitude profiles of T, RH and vapour isotopes for a given day  
167 as input parameters. The drop is assumed to form in equilibrium (at RH=100 %) at a level which differs from  
168 day to day. The input parameters for the vapour can be introduced into the BCIM in two different ways: (1) the  
169 profiles can be calculated based on assumption of idealized (moist) adiabatic ascent of an air parcel from the  
170 surface to the top of the column; RH, T and vapour isotope values at various pressure levels are then estimated  
171 from the Rayleigh distillation equations starting from the measured surface values or (2) the height specific  
172 values of RH and T from radiosondes and vapour isotope values from satellite data and/or any model.

173 Since our aim is to understand the isotopic modification and mass loss suffered by the drops by rain  
174 vapour exchange, the discussion is simplified if we introduce two parameters indicating the deviation of the  
175 final rain composition at the ground from the ambient surface vapour (Graf et al. 2019). This is most clearly  
176 expressed by the difference between the isotopic composition of vapour in equilibrium with the rain samples  
177 (rain eq. vapour) and the ambient surface vapour defined as:  $\Delta\delta = \delta D (\text{rain eq. vapour}) - \delta D (\text{surface vapour})$   
178 and similarly for d-excess,  $\Delta d = d\text{-excess (rain eq. vapour)} - d\text{-excess (surface vapour)}$ .

179

### 180 **2.4.1 Drop size assignment**

181 For calculating the drop evolution, the model requires the input diameter of the initial hydrometeor.  
182 Unfortunately, no disdrometer or micro rain radar observations are available for Pune during 2019. We,  
183 therefore, adopted the well-known Marshall-Palmer distribution (Marshall and Palmer, 1948), to estimate the  
184 mean drop size at the ground. First, we calculate the hourly mean drop size of the raindrops from the hourly rain  
185 rate data, available from the IMD observatory at Shivajinagar, Pune, located about 4 km away from the  
186 sampling location. Next, we calculate the 24-hour mean drop size by taking a weighted average of the size using  
187 rain rates as the weights. The calculated drop sizes at the ground vary from 0.61 mm to 1.80 mm for the 29  
188 sampling days. The drop diameter at the ground is next provided as an input, and the drop size at the drop  
189 introduction height (about 2.0 km above ground) is estimated iteratively in BCIM using the microphysics part of

190 the model. This procedure was adopted for each day. The accuracy of the drop size based on the Marshall-  
191 Palmer distribution and the rain rate is limited, but this was the only option available to us. Our choice was  
192 guided by earlier modelling and observational studies where the Marshall-Palmer distribution has been used  
193 (Graf et al., 2019; Sarkar et al., 2023; Morrison et al., 2020; Ryu et al., 2025; Jiang et al., 2024).

194

#### 195 **2.4.2 Drop formation height assignment**

196 In a simplified picture, the drop formation height would correspond to the most probable altitude range  
197 where the majority of the drops exist on any given day. This is not known a priori and was inferred from the  
198 CLWC analysis (See SI-5). The CLWC is defined as the total mass of liquid water droplets suspended in a unit  
199 volume of air within a cloud, typically expressed in grams per cubic meter or per kilogram of dry air. An earlier  
200 study by Kumar et al. (2014) showed that a peak of CLWC is often present at about 850 mb during the monsoon  
201 season over western India. In the present case, the CLWC profiles for 29 days of the study period, obtained from  
202 the ERA5 dataset, show peak values lying within  $830 \pm 70$  mb, i.e., about 1650 m above mean sea level (See  
203 Table S5-1 and Fig. S5-1). Here, we consider the CLWC peak of a given day as the drop introduction height for  
204 that day.

205 Clouds comprising small-sized water droplets form by condensation above a certain base height where  
206 the vapour pressure equals the saturation vapour pressure. We can consider the cloud base height to be the  
207 Lifting Condensation Level (LCL) where RH attains 100%. The RH and T profiles from the radiosonde data at  
208 various heights (with extrapolated ground level values; see SI-6b) can be used to estimate the LCL using the  
209 Skew T-Log P diagram for all 29 sampling days. The LCL varies from 820 to 900 mb, and the average height is  
210  $890 \pm 20$  mb (about 1050 m; see Table S5-1). We notice that the LCL is always below the corresponding day's  
211 CLWC peak (by about 600 m on average) and therefore, the drop falls through a zone of 100% RH till it  
212 emerges below the cloud base at LCL (see SI-5) where it falls through a zone of RH less than 100%.

213

#### 214 **2.4.3 Isotopic composition of the ambient vapour and hydrometeor**

215 The isotopic composition of the ambient vapour at various heights is not known a priori. They are  
216 estimated from one of several possible sources and vary depending on the inherent assumptions. Three types of  
217 profiles were considered in this work, one after another, with the idea of improving the BCIM predictions to  
218 match the observed rain isotope results. To clearly present how this was done, we discuss the vapour isotope  
219 profiles along with the results for each choice in the Results section (Section 3.2.1 to 3.2.4; Table 1; See also SI-  
220 6 and SI-7).

221 Once the vapour isotopes are fixed, the initial composition of the introduced hydrometeor is calculated  
222 by assuming formation in equilibrium from the vapour at this altitude and the ambient temperature.  
223 Subsequently, the composition of the falling hydrometeor at lower altitudes is calculated by using isotope mass  
224 balance and diffusive transport associated with exchange with the surrounding vapour involving appropriate  
225 fractionation factors (Graf et al., 2019).

226 The mass and temperature of the hydrometeor are calculated along its fall trajectory using the equations  
227 governing the microphysics of the falling hydrometeor (Foote and du Toit, 1969; Pruppacher and Klett, 2010).  
228 The temperature, pressure, and RH values are interpolated from the adopted profiles in various runs. It is  
229 important to mention here that many processes considered in the original BCIM (e.g., ice formation, vapour

230 deposition, rimming) do not occur for the shallow convective clouds in Pune (Utsav et al., 2017). Therefore, the  
231 BCIM inputs need to be considered only up to the drop introduction heights (see Table 1). The model also does  
232 not consider downdraft or advection of air masses. The inputs for various simulations are obtained from several  
233 possible sources given in Table 1 and discussed in Section 3.2.

234

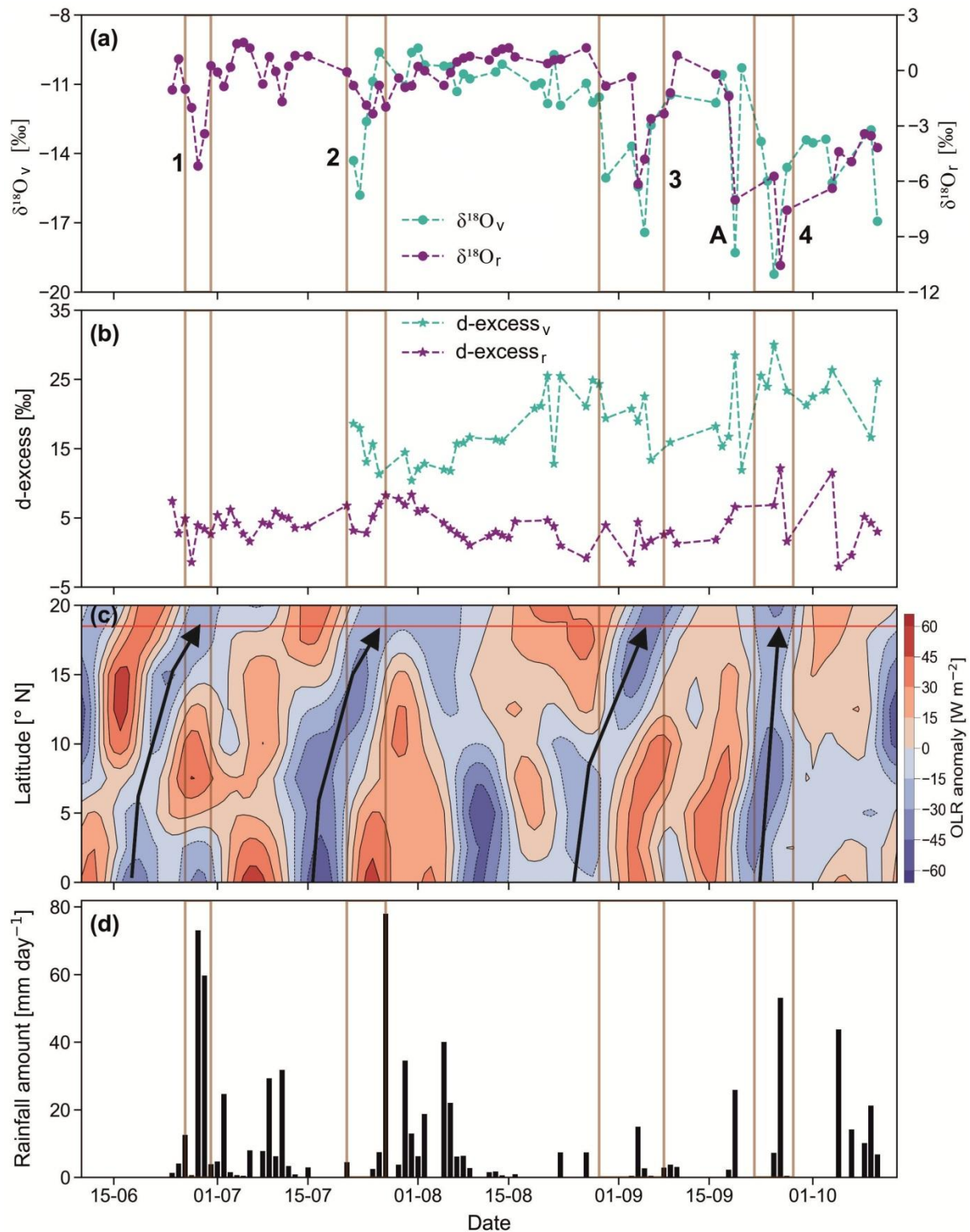
### 235 3. Results

236 We present the results of the current study broadly in two sections: (1) Results of isotope analysis and  
237 (2) Results of BCIM simulations. The first section presents the measured isotope ratios in the context of  
238 meteorological parameters, whereas the BCIM simulations are compared with the measured values in the second  
239 section.

240

#### 241 3.1 Results of isotope analysis

242 Measured rain and vapour isotope ratios ( $\delta^{18}\text{O}$  and d-excess) on a daily scale are plotted in Fig. 2a and  
243 2b. The general pattern of variations in vapour  $\delta^{18}\text{O}$  ( $\delta^{18}\text{O}_v$ ) and rain  $\delta^{18}\text{O}$  ( $\delta^{18}\text{O}_r$ ) values is similar; both decrease  
244 significantly and consistently after mid-August. The vapour  $\delta$ -values are lower than the rain. In contrast, the d-  
245 excess values of vapour ( $d_v$ ) are always much higher. The  $\delta^{18}\text{O}_r$  and d-excess ( $d_r$ ) values of rainwater range from  
246  $-10.8\text{‰}$  to  $1.5\text{‰}$  and  $-2\text{‰}$  to  $12\text{‰}$ , respectively, while those of the vapour range from  $-19\text{‰}$  to  $-9\text{‰}$  and  
247  $10\text{‰}$  to  $30\text{‰}$ , respectively. The mean and  $1\sigma$  standard deviation of  $\delta^{18}\text{O}_r$  and  $d_r$  values are  $-1.3\pm 2.6\text{‰}$  and  
248  $3.9\pm 2.7\text{‰}$ , while those of the vapour are  $-12.5\pm 2.5\text{‰}$  and  $18.3\pm 5.2\text{‰}$ , respectively. The  $\delta^{18}\text{O}$  (Fig. 2a) and d-  
249 excess (Fig. 2b) time series show four interesting features: (1) For the four date ranges: 27-29 June, 24-27 July,  
250 4-8 September, and 19-27 September, significant and consistent decrease in isotope values are observed in both  
251 rain and vapour phases (marked 1, 2, 3, 4 in Fig. 2a; no vapour data available for date range 1), (2) On 19  
252 September, the vapour shows a sudden decrease (marked A in Fig. 2a), (3) there is a gradual decrease in vapour  
253  $\delta^{18}\text{O}_v$  values and an increase in d-excess values with the progress of the monsoon, which is especially prominent  
254 in the later part, and (4) rain d-excess ( $d_r$ ) values remain constant with time but  $\delta^{18}\text{O}$  of both rain and vapour  
255 start decreasing beginning from early September.

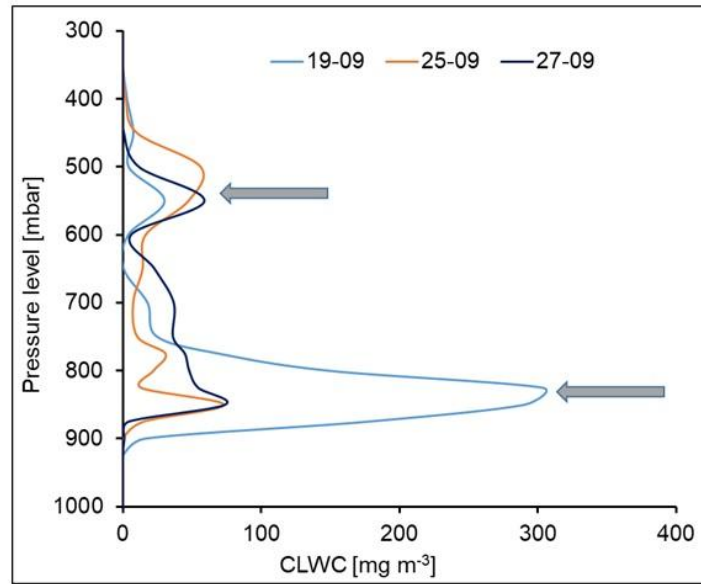


256

257 **Figure 2.** The time series of (a)  $\delta^{18}\text{O}$  and (b) d-excess values of the rainwater and water vapour, denoted by  
 258 subscripts r and v, respectively. (c) OLR anomaly ( $\text{W m}^{-2}$ ), and (d) daily rainfall (mm over 24 h) in Pune. The  
 259 four vertical boxes (numbered 1, 2, 3, and 4) denote synchronous low OLR values and low isotope values (i.e.,  
 260 less than their respective  $\mu-0.5\sigma$  values). These periods are defined as low-isotope events. The label A indicates  
 261 one isolated low isotope value without a negative OLR anomaly. Thick arrows show how convective cloud  
 262 bands (indicated by low OLR anomaly) traverse to the sampling region over Pune from the southwest. Note  
 263 highly depleted values on 19, 25 and 27 September.  
 264

264

265



266

267 **Figure 3.** Presence of second CLWC peaks at higher altitudes (about 550 mb) on 19, 25 and 27 September 2019  
 268 (beside the first major peaks at lower altitudes) when highly depleted  $\delta^{18}\text{O}_r$  values were observed in association  
 269 with negative OLR anomaly (see Fig. 2). The altitudes of the two sets of peaks are shown by two arrows. The  
 270 data for the plot is obtained from ERA5.

271

272 Isotopic depletions in rain and vapour samples in the tropics are often associated with deep convection  
 273 (Lekshmy et al., 2014; Risi et al., 2008; Sengupta et al., 2020). Signature of such a phenomenon is possibly  
 274 present here in the form of depleted-isotope events when isotope ratios of a group of samples fall below the  
 275 overall mean ( $\mu$ ) minus half the standard deviation ( $\sigma$ ) (Sengupta et al., 2020). To find the relation of these  
 276 events to large convective episodes, a latitude-time Hovmoeller plot of daily OLR anomaly (averaged over the  
 277 longitude  $70^\circ\text{ E}$  -  $75^\circ\text{ E}$ ) is examined in Fig. 2c. The OLR values are often used as a proxy for convection  
 278 because the cloud top temperatures, being an indicator of cloud height, a negative OLR anomaly means colder  
 279 cloud top temperatures or greater cloud thickness. This, in turn, implies extensive coverage by deep cloud  
 280 systems, characteristic of mesoscale convection. A time synchronous association of low OLR and depleted-  
 281 isotope events thus indicate mesoscale convection affecting isotope values. Fig. 2c indicates four such isotope-  
 282 depleting mesoscale events (marked as 1, 2, 3 and 4 in Fig. 2a). In addition, we also see one depleted-isotope  
 283 event without such association (marked as A in Fig. 2a). Interestingly, prominent second CLWC peaks occurred  
 284 on three days, 19, 25 and 27 September, at much higher levels (about 550 mbar or about 5.5 km altitude; see  
 285 Fig. 3) corresponding to the event number 4 mentioned above.

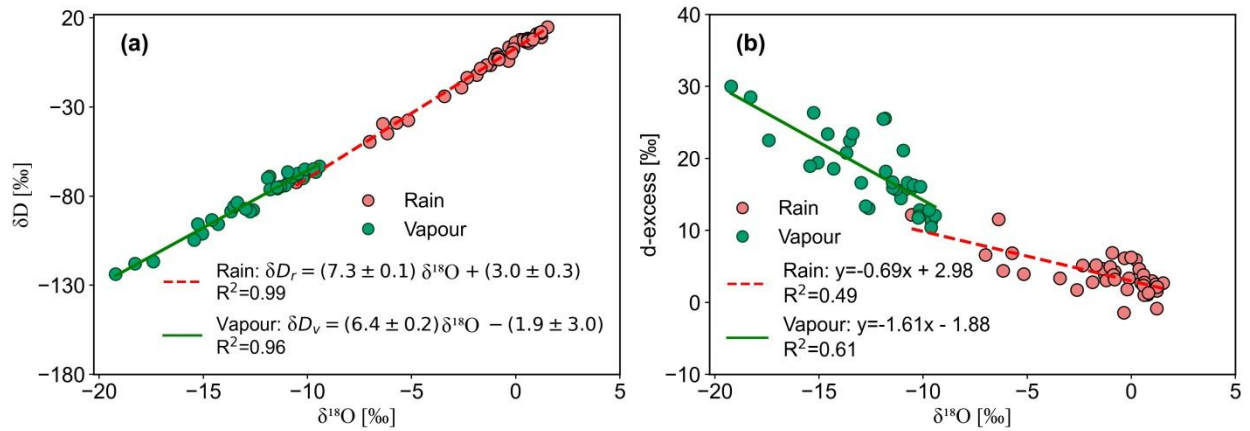
286

287 Fig. 2d shows that major rainfall occurred during the months of July and August. The relative humidity  
 288 at the surface during the whole monsoon season varied from 71 % to 97 %, and the surface temperature varied  
 289 from  $25^\circ\text{ C}$  to  $30^\circ\text{ C}$  (see Fig. S6-2). It is evident from Fig. 2d that deep convection is associated with high  
 290 rainfall for the three events 1, 2, and 4. A recent study, based on a year-long continuous measurement of  
 291 atmospheric vapour in Sri Lanka (a nearby tropical country with a similar monsoon system), also found such  
 isotopic depletion during high rainfall events (Wu et al., 2025).

292 Fig. 4a shows the Local Meteoric Water Line (LMWL) using rainwater samples and the Local Water  
 293 Vapour Line (LWVL) using vapour samples from this study. The LMWL equation is  $\delta D_r = (7.3 \pm 0.1) \delta^{18}O +$   
 294  $(3.0 \pm 0.3)$  and the LWVL,  $\delta D_v = (6.4 \pm 0.2) \delta^{18}O - (1.9 \pm 3.0)$ , subscripts r and v denote rain and vapour. The slope  
 295 and intercept of the LMWL values are lower than those of the Global Meteoric Water Line (GMWL), which are  
 296 8.0 and 10.0, respectively (Dansgaard, 2012; Gat, 1996). This difference, though small, suggests some amount  
 297 of below-cloud evaporation of the rain. At Roorkee, a high-latitude Indian station, Saranya et al. (2018) found a  
 298 LMWL with a lower slope (5.4) but a higher intercept (27). They attributed these changes to the contribution of  
 299 evaporation from water bodies nearby and moisture recycling during the monsoon. Rahul et al. (2016) got a  
 300 similar slope (7.4) but a lower intercept (1.5) in Bangalore (southern central India, at a high altitude of ~1000  
 301 m). The lower slopes of meteoric water lines provide a signature of evaporation processes associated with  
 302 kinetic fractionations occurring during rain.

303 The d-excess values of rain samples suffering evaporation generally bear a negative relationship with  
 304  $\delta^{18}O$  values (Bonne et al., 2014; Munksgaard et al., 2020). Such an effect is clearly seen in our data (Fig. 4b). In  
 305 addition, the vapour d-excess values also show a statistically significant negative correlation with  $\delta^{18}O$  values  
 306 (Fig. 4b;  $R^2 = 0.61$ ;  $p = 0.001$ ), probably indicating contribution of vapour derived from rain evaporation  
 307 (Kurita, 2013; Risi et al., 2021). Correlation studies can be indicative, but the causative factors behind the above  
 308 variations can be explored only with the help of a process-based model like BCIM.

309  
 310



311  
 312 **Figure 4.** A cross-plot of (a)  $\delta D$  and  $\delta^{18}O$  of rain and vapour; (b) a cross-plot of d-excess and  $\delta^{18}O$  of rain and vapour  
 313 showing anti-correlation. The regression equations and correlation coefficients are shown inside the plots.

314

### 315 3.2 Results of BCIM simulations

316 As discussed in section 2.4, simulation runs of BCIM were carried out under three assumptions about  
 317 the vertical profiles of RH, T and vapour isotopes. The results are shown as Run-1, Run-2 and Run-3, which  
 318 were designed to make progressive improvement in reproducing the measured rain isotope values by altering the  
 319 input parameters. The sources of input profiles of ambient temperature (T), relative humidity (RH), vapour  $\delta D$   
 320 ( $\delta D_v$ ), and vapour d-excess ( $d_v$ ) required for the three BCIM runs are given in Table 1.

321  
 322  
 323

324 **Table 1.** Input parameters for various BCIM runs  
 325

Sl. No	BCIM input	Parameters for Run-1	Parameters for Run-2	Parameters for Run-3
1	Drop size	Marshall-Palmer equation using hourly rainfall data obtained from IMD	Same as Run-1	Same as Run-1
2	RH profile	Rayleigh ascent ~15 % increase per km and 100% above CBH to drop introduction height	Radiosonde values normalized to surface observation and changed to 100% above CBH to drop introduction height	Same as Run-2
3	Temperature profile	Rayleigh ascent Lapse rate ~ 5.6°C km <sup>-1</sup>	Radiosonde normalized to ground value	Same as Run-2
4	δD <sub>v</sub> profile	Rayleigh ascent ~7 ‰ decrease per km	TES normalized to measured surface value	δD <sub>v</sub> values reduced slightly (within ±4‰), keeping the shapes like Run-2
5	d <sub>v</sub> profile	Rayleigh ascent ~0.1 ‰ increase per km	LMDZ δD <sub>v</sub> and δ <sup>18</sup> O values used to get d <sub>v</sub> normalized to the measured ground value	d <sub>v</sub> decreased from Run-2 average of 17‰ to an average ~10‰
6	Rain drop formation height (CLWC peak)	ERA5 CLWC peak	Same as Run- 1	Same as Run- 1
7	Cloud Base Height (LCL)	LCL from radiosonde profiles using skew-T log P diagram	Same as Run-1	Same as Run-1

326

### 327 3.2.1 Run-1: Rayleigh ascent results

328 In Rayleigh simulations (Run-1), the profiles were calculated using the equations for moist-adiabatic  
 329 ascent of air parcels (following Appendix A1 of Graf et al., 2019), starting at the surface vapour values of T,  
 330 RH, δD<sub>v</sub> and d<sub>v</sub> of each sampling day as inputs. The values of δD<sub>v</sub> and d<sub>v</sub> were taken from our own surface  
 331 vapour measurements, whereas the daily average T and RH values were obtained from the surface observations  
 332 of IMD (Section 2.3). A dry adiabatic ascent formula is used up to the cloud base (LCL). Above the cloud base,  
 333 a moist-adiabatic lapse rate is used. These input profiles for the 29 sampling days are given in SI-6 (Fig. S6-2  
 334 and Fig. S6-3).

335 Results of Run-1 (Rayleigh ascent) simulations are compared with the observed values of δD<sub>r</sub> (Fig.  
 336 5a), δ<sup>18</sup>O<sub>r</sub> (Fig. 5b), and d<sub>r</sub> (Fig. 5c) values. We also construct Δδ–Δd cross plots for both observed and model  
 337 values in Fig. 5d. Although observed and model isotope values (Fig. 5a and 5b) show strong correlation  
 338 (R<sup>2</sup>=0.86 and 0.79, respectively), the model values deviate (the plotted points deviate from the 1:1 line). The  
 339 mismatch in estimation of rain isotopes (for δ<sup>18</sup>O<sub>r</sub> and δD<sub>r</sub>) affects the d-excess values considerably more; the  
 340 points lie far to the right, and no correlation exists between the observed and model d-excess values (Fig. 5c).  
 341 This is because the d-excess parameter is highly sensitive; even a small departure in δ values magnifies the  
 342 discrepancy in d-excess. Most of the model data points in the Δδ–Δd cross-plot do not agree with the observed  
 343 data points and lie closer to the origin. Many of the model points fall in the lower right quadrant, indicating the

344 presence of strong raindrop evaporation. We also note that the model  $\Delta\delta$  and  $\Delta d$  values (Fig. 5d) show smaller  
345 variations compared to the observations. The  $\Delta\delta$  of the model simulations varies from 0 ‰ to 5 ‰ and  $\Delta d$  from  
346 0 ‰ to -5 ‰, while the observed values have variations of about 25 ‰ (higher by a factor of 5). These  
347 comparisons show that the Rayleigh ascent model with the chosen inputs fails to reproduce the evolution of the  
348 rain isotopes in our region. We suspect that the vertical profiles of RH, T and vapour isotopes need to be  
349 modified to improve the simulations. Rayleigh ascent in Run-1 assumes that the source of vapour aloft is an  
350 unaltered rising air parcel with constant specific humidity. But we see from Fig. S5-2 and S6-2 that this  
351 condition results in unusually low cloud base over Pune (i.e., the level where RH attains the value of 100%),  
352 inconsistent with observations (Naik et al., 2003). In fact, the radiosonde data show that specific humidity  
353 decreases with height (see SI-7; Fig. S7-1b). It is well known that a decrease in specific humidity is associated  
354 with a decrease in vapour isotope ratios (Noone, 2012; Worden et al., 2007; see SI-7 for details). Moreover, in  
355 Run-1, the isotopic inputs for the BCIM isotope lapse rates are taken from the measured surface  $\delta D_v$  and  $d_v$ . But  
356 these vapours are influenced by downdrafts associated with rain events. The downdrafted air brings down  
357 vapour with lower isotope ratios contributed by rain evaporation. Therefore, the post-rain vapour values are not  
358 representative of the atmospheric column before droplets form, precipitation falls, and rain evaporation occurs.  
359 To improve the model predictions, we change the profiles in Run-2 simulations (given below).

360

### 361 **3.2.2 Run-2 results**

362 The failure of the Rayleigh ascent method (Run-1) prompted us to explore other sources of vertical  
363 profiles of RH, T and vapour isotopes. Instead of the Rayleigh ascent method, RH and T profiles are now taken  
364 from the radiosonde (section 2.3) and vapour isotope from TES as discussed below.

365

#### 366 **(a) Mean vertical profiles of vapour isotopes from TES and LMDZ**

367 To obtain the vertical profiles of vapour isotopes, we first tried out a particular General Circulation  
368 Model, LMDZ. The output data for our sampling days over Pune was provided by Dr. Camille Risi (personal  
369 communication, 2023) using the LMDZ isotope-enabled general circulation model, known as LMDZ-iso (Risi et  
370 al., 2010), which is a version of the LMDZ atmospheric model adapted to simulate the natural variations of  
371 water isotopes in precipitation and vapour. Unfortunately, when the vapour isotope values from LMDZ-iso over  
372 Pune are used as inputs to BCIM, the model values did not yield good agreement with observations (results not  
373 shown). Therefore, in the next attempt, we used the measured  $\delta D_v$  profiles obtained from Tropospheric  
374 Emission Spectrometer (TES) pertaining to the Pune region. However, the TES data were available only for  
375 2005-2009. For our study year of 2019, we assumed that the time discrepancy can be accounted for if the final  
376 profiles are approximated by using the measured daily-scale surface vapour isotope ratios as a boundary  
377 constraint while maintaining the shapes of the TES  $\delta D_v$  profiles.

378 We should mention here that apart from TES,  $\delta D_v$  data, in principle, can be obtained from one other  
379 source, namely, the Atmospheric Infrared Sounder (AIRS) (see SI-8). However, isotope vertical profiles  
380 obtained from AIRS and used in the BCIM (after suitable boundary constraints) produced model rain values that  
381 were widely different from the observed values. The possible causes for this are explored in SI-8.

382 The derivation of TES isotope profiles assumes that the shapes of the TES average profiles were  
383 applicable as far as the vertical variation is concerned. The TES satellite provides  $\delta D_v$  values of moisture at 17

384 pressure levels with a 5.3 km × 8.4 km footprint during the years 2005-2009 over a box covering the study  
385 region (16°-20° N; 72°-76° E). Using these data sets, we can derive an average TES profile and assume it to be  
386 representative of the shape of the mean ISM (June-September) profile. Our station at Pune falls within the  
387 above-mentioned box, but there is an inherent assumption that the average over a ~45 km<sup>2</sup> area represents the  
388 vapour over a small sampling location if we force the boundary constraint. Under this constraint, the TES  
389 average profile is adjusted to match the measured ground vapour value at the sampling location. A support for  
390 this assumption is provided by the back-trajectory analysis that indicates that the Pune moisture source is always  
391 from the Arabian Sea (see Fig. S4-1). Interestingly, an average  $\delta^{18}\text{O}_r$  value of rainwater in Bombay (from 1961  
392 to 1978) is -1.3 ‰ (Bhattacharya et al., 2003), close to the Pune average value of -1.1 ‰ from the present study.  
393 It shows that Pune, being located 150 km downstream of Bombay, receives moisture of similar composition as  
394 Bombay (with potential addition from the evaporation component on the way). Therefore, our assumption of a  
395 large spatial average representing a small location is not expected to be wrong, at least as far as the vertical  
396 variation is concerned.

397

#### 398 **(b) Daily scale profile by adjustment technique**

399 As mentioned, the  $\delta D_v$  and  $d_v$  profiles for each date from the TES data were obtained by adjustment  
400 with the measured surface values. We analyzed the available TES  $\delta D_v$  profiles for the years 2005-2007 and  
401 derived three profiles which correspond to the minimum, mean and maximum surface  $\delta D_v$  values. Each of these  
402 three profiles was fitted with polynomials, and the coefficients of these polynomials were treated as functions of  
403 the surface values. Once we get these functions, we can obtain the vapour isotope profiles for any day by using  
404 that day's surface value. This exercise was necessary to translate the variation of the discrete TES values into an  
405 analytical form, allowing for easy calculation of vapour isotope values at each height (at one meter resolution)  
406 from the drop introduction point to the ground level.

407 A similar exercise was conducted to obtain the daily  $d_v$  profile from the LMDZ output and normalizing  
408 the profile to the measured  $d_v$  value. In brief, this was done by using the available  $\delta D_v$  and  $\delta^{18}\text{O}$  profiles from  
409 LMDZ output for three cases (Mean, Max and Min surface values), fitting 4<sup>th</sup>-order polynomials:  
410  $Ah^4+Bh^3+Ch^2+Dh+E$ , and then constructing the d-excess profiles for three cases with five coefficients. Five  
411 coefficients were used to get higher precision in fitting. Again, fitting was done for each of the polynomial  
412 coefficients (A, B, C, D and E) as a function of surface value. Using the coefficients,  $d_v$  profiles are obtained for  
413 each day. This procedure is discussed in detail in SI-6a. Fig S6-2 and Fig S6-3 show the input profiles (RH and  
414 T), and ( $\delta D_v$  and  $d_v$ ) respectively, for the three runs: Run-1, Run-2 and Run-3. The method of estimating the  
415 vapour profile, constrained by surface vapour measurements, assumes that the vapour aloft is related to the  
416 surface value. This assumption may not be strictly correct, but it allows us to check whether the BCIM, under  
417 the surface constraints, yields better rain isotope ratios compared to the Rayleigh model while being consistent  
418 with the TES measurements of vapour aloft.

419 The above profiles were employed in BCIM (Run-2) to generate the daily-scale  $\delta^{18}\text{O}_r$ ,  $\delta D^r$  and  $d_r$   
420 values of surface rain (Fig. 5e-5h). However, the results do not show much improvement compared to the Run-1  
421 (Fig. 5e-5g) despite showing a larger variability in the  $\Delta\delta$ - $\Delta d$  plot (Fig. 5h); the  $\Delta\delta$  values varied from -4.7 ‰  
422 to 11 ‰ and  $\Delta d$  from -1.8 ‰ to -12.4 ‰. As in Run-1, all the model data points fell in the lower right quadrant  
423 of the  $\Delta\delta$ - $\Delta d$  cross plot (Fig. 5h and Fig. 5d). In conclusion, both Run-1 and Run-2 simulations fail to yield a

424 good match with the model values (especially the d-excess). The  $\delta D_r$  values differ by about -8 ‰ to 20‰, and  
425 the model d-excess values are higher (by 0 to 15 ‰). Interestingly, the model rain values of Run-1 and Run-2  
426 are quite close (within  $\pm 2.5$  ‰) despite RH, T,  $\delta D_v$  and  $d_v$  profiles being very different. This suggests that the  
427 assumption of surface vapour value as the boundary constraint, as used in both these runs, is the main  
428 determinant for rain isotopes.

429

### 430 3.2.3 Possible sources of failure in predictions of Run-1 and Run-2

431 The failure of Run-1 and Run-2 predictions, as discussed above, indicates that we still need to modify  
432 the input profiles to obtain a good match with the observed values. It is easy to see that the ambient vapour  
433 isotope values have the maximum impact on the model rain isotope values. This can be shown quantitatively by  
434 a multiple regression analysis of rain isotope values with four influencing factors (RH, T, surface  $\delta D_v$  and drop  
435 diameter) in their normalized forms. The normalized values (the ratio of anomalies of the daily data and  $1\sigma$   
436 standard deviation) of the model rain isotope ratios  $\delta D_{\text{mod-rain}}$  obtained from Run-2 for the 29 sampling days  
437 were regressed with the normalized values of the above-mentioned four variables. We obtain the following  
438 multiple regression equation (normalized):

439

$$440 \delta D_{\text{mod-rain}} = -0.114 * RH + 0.035 * T - 0.059 * \text{drop diameter} + 0.986 * \delta D_v \quad (1)$$

441

442 This equation indicates that the major influence on the model rain isotope value is from the ambient  
443 vapour  $\delta D_v$  (with a coefficient of nearly one, meaning +1 ‰ change in  $\delta D_v$  would result in +1 ‰ change in the  
444 rain  $\delta D_r$ ). In contrast, the influence of RH, for example, is only one-tenth in the opposite direction. The  
445 influences of T and droplet size are still less. It is logical to assume that the main source of discrepancy in Run 2  
446 simulations is improper vapour isotope profiles and therefore, for tuning, a change in the vapour isotope value  
447 would be the most effective.

448 It seems that the true profile for a given date does not coincide with the adopted one based on  
449 extrapolating to the measured surface value, as assumed by the boundary constraint. In other words, the vapour  
450 aloft may not be derived entirely from the surface vapour as measured at our sampling location. The reason for  
451 this could be a significant contribution from the local surface moisture having a different isotopic composition  
452 (evaporation or evapotranspiration from water bodies or trees within a few hundred meters). However, this  
453 possibility can be ruled out as a study using satellite data showed that, due to high humidity during the monsoon  
454 season, evaporation/ evapotranspiration ( $\sim 0.5 \text{ mm day}^{-1}$ ) adds a negligible amount of moisture compared to the  
455 advective flux in this region (Pathak et al., 2014). In this context, we note that the measured surface vapour  
456 refers to post-rain ground-level vapour, which may suffer from downdrafted vapour with contributions from  
457 drop evaporation. This contribution may change the surface vapour when we measure it, making it different  
458 from the vapour that gave rise to the raindrops aloft. However, this suggestion is based on a  
459 posteriori reasoning and invoking downdrafted evaporation-generated vapour as a possible source is a  
460 speculation.

461

462

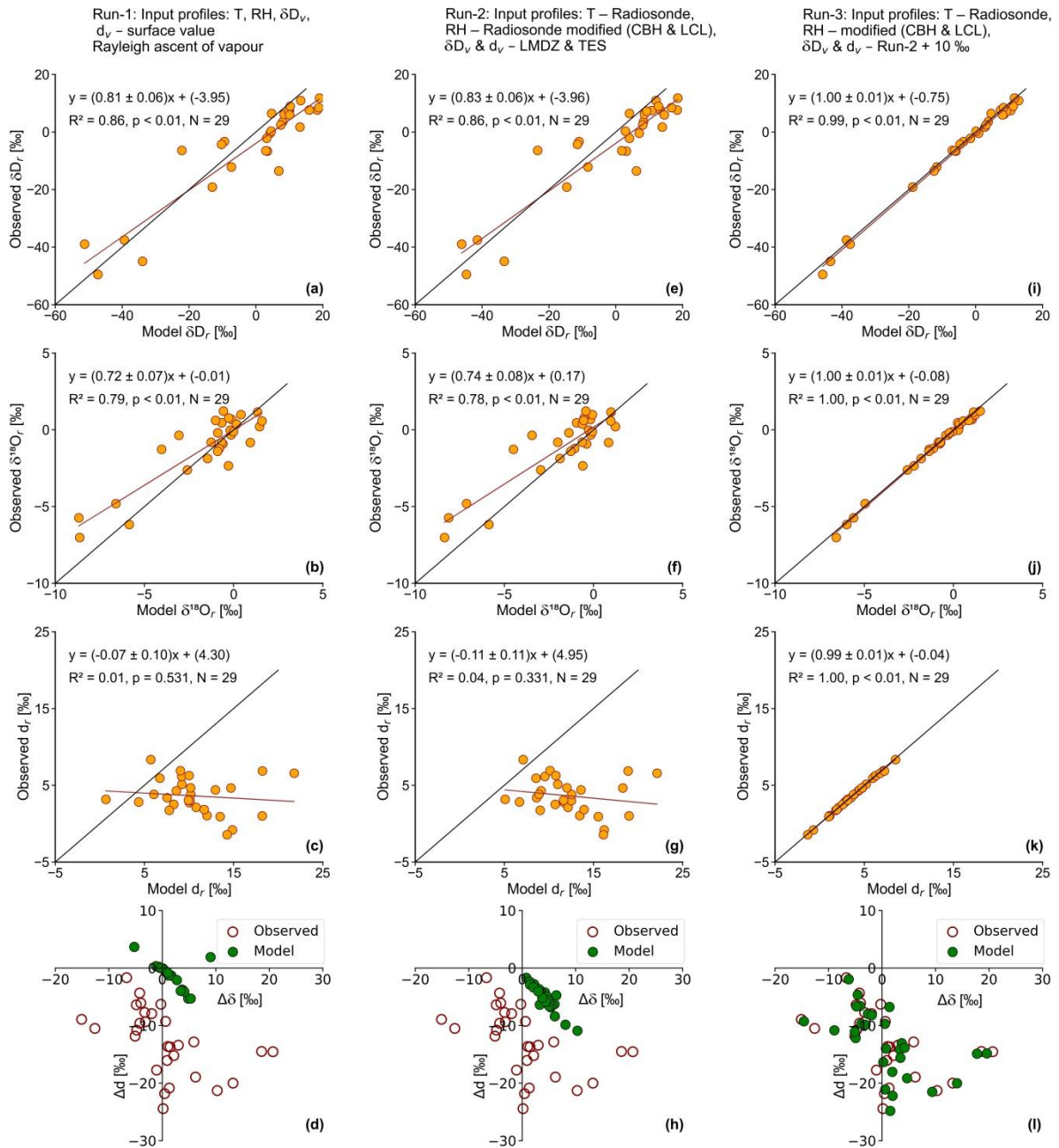
463

464 **3.2.4 Run 3 results**

465 Guided by the regression equations, we tuned the vapour  $\delta D_v$  and  $d_v$  input profiles (Run-3) to achieve  
466 a better agreement in the rain isotope values for each date (Fig. 5i-5k). The surface  $\delta D_v$  values were changed by  
467 amounts varying from +13.9 ‰ to -17.8 ‰, and the  $d_v$  values from +3.2 ‰ to -17.1 ‰ while keeping the shape  
468 for daily profiles similar to Run-2. Corresponding changes in the vapour  $\delta^{18}O$  were from +2.9 ‰ to -1.9 ‰.  
469 Most of the changes were small; in the  $\delta D_v$ , 23 out of 29 changes were within  $\pm 4$  ‰ and in the  $d_v$  23 out of 29  
470 changes were within  $\pm 3.4$  ‰. As a consequence of this tuning, the average  $d_v$  of the surface vapour decreased to  
471 10.7 ‰ from the average measured value of 17.3 ‰. The resultant vapour isotope profiles of Run-3 are shown  
472 along with those of Run-1 and Run-2 in Fig. S6-3. As designed, this tuning resulted in good agreement of the  
473 model values with the observed values. A two-tailed Student's t-test shows that the Run-3 model values are  
474 close to the observed surface rain isotope values for all three parameters ( $\delta^{18}O_r$ ,  $\delta D_r$ , and  $d_r$ ) at  $p=0.05$   
475 significance level (see SI-9; Table S9). The average (observation-model) d-excess difference decreases from 2.1  
476 to 0.4. Additionally, there is a close match in the  $\Delta\delta$ - $\Delta d$  cross plot (see Fig. 5l).

477 As mentioned above, the  $d_v$  value of the near-surface vapour measured during or post-rainfall, may  
478 have a substantial component of vapour from the rain evaporation zone in the sub-cloud layer. Therefore, the  
479 isotopic composition of the vapour is possibly different from that of the ground-level vapour measured. The  
480 downdrafted vapour should have d-excess values higher than the rain-forming vapour because raindrop  
481 evaporation generates vapour with lighter isotope ratios but higher d-excess. So, when we measure isotopes in  
482 vapour post-rainfall, we have an artifact due to variable addition of downdrafted vapour with high d-excess. The  
483 contribution cannot be estimated easily, and it is variable. The vapour isotope values during the monsoon days  
484 change from day to day and do not have a fixed value. Therefore, we cannot take any non-rainy-day value as  
485 proxy for an unaltered vapour which is responsible for the rain formation.

486  
487



488

489

490 **Figure 5.** Scatter plots showing observed vs model values for rain  $\delta D_r$ ,  $\delta^{18}O_r$ , and  $d_r$  for various runs (Run-1, Run-2 and  
 491 Run-3) of BCIM in the upper nine panels. The bottom three panels show the  $\Delta\delta$ – $\Delta d$  cross-plots for the runs. The input  
 492 profile sources of T, RH, vapour  $\delta D_v$  and  $d_v$  used in the model for the three runs are given in the descriptions above. The best  
 493 agreement between the observed and model values is achieved in Run-3. Run 3 uses the same RH and T as Run 2, but  $\delta D_v$   
 494 and  $d_v$  values are adjusted by tuning. The average  $d_v$  reduces to 10.7 ‰ from the observed value of 17.3 ‰ used in Run-2.  
 495

### 496 3.2.5 Sensitivity and uncertainty based on Run-3 predictions

497 We conducted an uncertainty analysis (see SI-10) and a sensitivity analysis (see SI-11) of the model  
 498 rain composition using Run-3 results to study the effects of variation in vapour isotopes ( $\delta D_v$ ), relative humidity  
 499 (RH), temperature (T), and drop diameter (D). We find that the vapour isotope value is the most important factor  
 500 controlling rain isotope ratios in the BCIM. The uncertainty of the model predicted  $\delta D_r$  and  $d_r$  are 3.0 ‰ and 1.7

501 ‰, respectively. In case of sensitivity, for a +10 % change over the reference values of the parameters,  $\delta D_v$ , RH,  
502 T and D, the changes in the  $\delta D_r$  values (in ‰) are: +7.6, -4.1, +2.6 and -0.4, respectively (Fig. S11-1).

503

#### 504 **4. Discussions**

505 For clarity, this section is divided into two major parts: (1) the discussion of the observed rain and  
506 vapour isotope ratios and what they mean, and (2) the message that we get by comparing the results of the  
507 BCIM with observations.

508

##### 509 **4.1 Influence of local meteorological parameters on observed isotope ratios**

510 In our data, the  $d_v$  is not significantly correlated with rainfall amount, relative humidity, specific  
511 humidity and temperature (details are provided in SI-12 and Fig. S12-1). However, we do see synchronous low  
512 OLR values and low isotope values (in both vapour and rain) as the convective cloud bands traverse to the  
513 sampling location in Pune from the southwest (Fig. 2).

514 Rain isotopes often vary with rainfall, humidity, and temperature (Dansgaard, 2012; Lee and Fung,  
515 2008). But the rain isotopes in Pune do not have a simple relation with the local rainfall (Fig. 2). The absence of  
516 rain amount-isotope correlation in the tropics has also been found in several other regions (Chakraborty et al.,  
517 2016; Moerman et al., 2013; Vimeux et al., 2011). Even though a straightforward relation with local rainfall is  
518 absent, a correlation is often found with the regional convective activities (Kurita, 2013; Lekshmy et al., 2018).  
519 Risi et al. (2023) have noted that in the tropics, most of the precipitation falls under deep convective systems  
520 (see Section 3.1 and Fig. 2), which are controlled by various microphysical processes (like rain evaporation,  
521 diffusive liquid-vapour exchanges) connected through mesoscale circulations. These processes probably add on  
522 to the effect of surface meteorological parameters in this region to offset a simple dependence of rain isotopes  
523 on rainfall. However, as noted above, movement of large-scale convective bands reflected by low OLR registers  
524 its signature in both low isotope events and high rainfall (Fig. 2).

525

##### 526 **4.2 Rain-vapour isotope exchange and rain evaporation**

527 The observed increasing trend (13 ‰ to 30 ‰) in the vapour d-excess values associated with a  
528 decrease in the  $\delta^{18}O$  values with the progress of the monsoon (Fig. 2b) is an intriguing feature and could be  
529 ascribed to a significant contribution from some evaporative sources. Changes in moisture sources can also  
530 cause concomitant changes in isotope values in rain and vapour (Deshpande et al., 2010; Midhun et al., 2018).  
531 We investigated this possibility by forty-eight hours of air-parcel back trajectory analysis (Fig. S4-1), which  
532 shows that moisture was derived mainly from the Arabian Sea throughout the season.

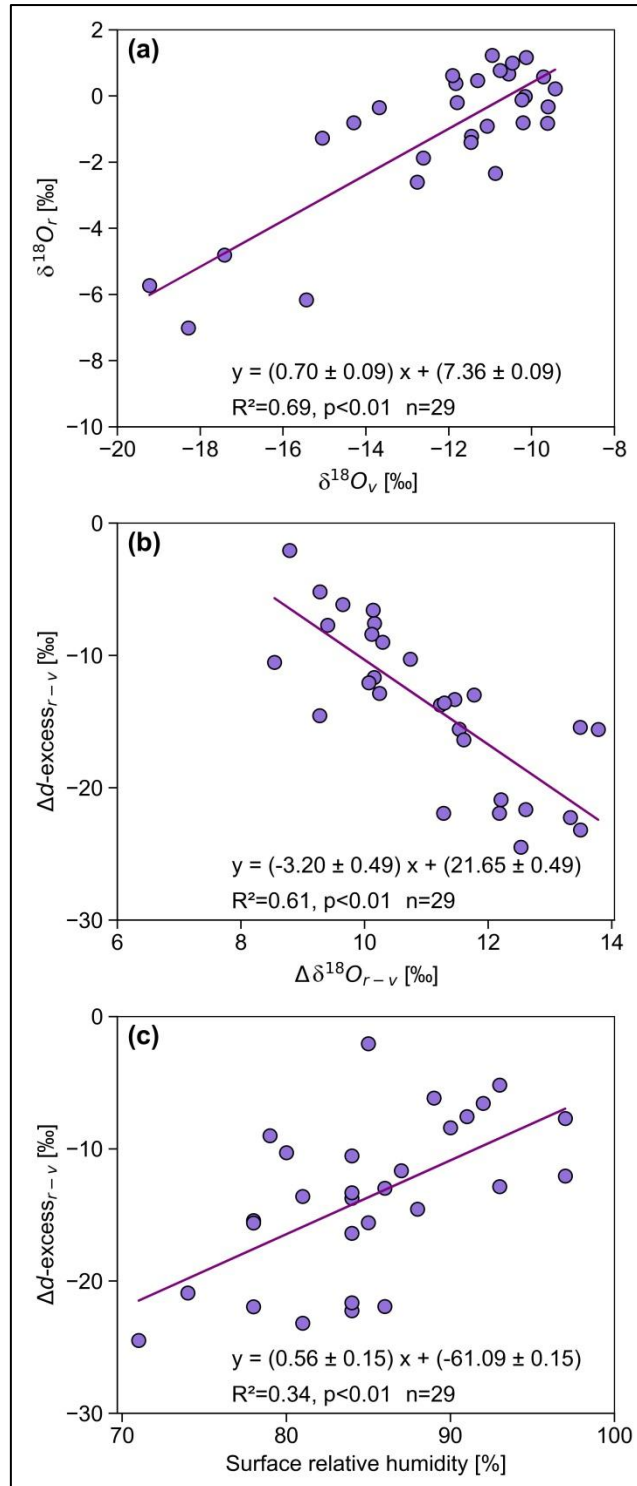
533 The process of evaporative exchange during the fall of raindrops causes isotopic enrichment in the rain,  
534 which cannot be easily quantified. Evaporation is reflected in higher  $\delta$ -values and lower d-excess values of the  
535 rain samples. Froehlich et al. (2008) used d-excess values of precipitation in the Alpine region to derive the  
536 extent of evaporation using assumed end-member values of the regional vapours. Any isotope exchange  
537 between the rain and ambient vapour would result in correlated changes. A strong correlation between rain and  
538 vapour  $\delta^{18}O$  values is indeed found (Fig. 6a;  $R^2=0.7$ ,  $p < 0.01$ ,  $n=29$ ). Sinha and Chakraborty (2020) also found  
539 significant positive relations ( $R^2>0.8$ ) between rain and vapour  $\delta^{18}O$  values over the Andaman Islands.  
540 However, they did not find any anti-correlation between  $\delta^{18}O_r$  and  $d_r$ , as found here (Fig. 4b). The current study

541 exhibits an anti-correlation between the differences in d-excess ( $\Delta d\text{-excess}_{r-v}$ ) and  $\delta^{18}\text{O}$  ( $\Delta\delta^{18}\text{O}_{r-v}$ ) of rain and  
542 vapour (the subscript r-v indicates rain isotope minus vapour isotope) (Fig. 6b).

543 As raindrops evaporate, part of the newly formed vapour may get down-drafted to lower levels; the rain  
544 and vapour phases at the ground level would exhibit opposite changes because the generated vapour is lower in  
545  $\delta^{18}\text{O}$  but higher in d-excess compared to the rain. This happens when the evaporative contribution is large.  
546 However, in the case of tropical precipitation, the fractional addition from rain evaporation is small because the  
547 ambient vapour is a large reservoir. It has been shown in several earlier studies that the total rain constitutes  
548 only a few percent of the overhead vapour mass (Pathak et al., 2014; Rahul et al., 2016). Earlier studies have  
549 also shown that vapour d-excess values do not exhibit any systematic change in central or southern WG stations,  
550 but their rain  $\delta^{18}\text{O}$  values exhibit slight but gradual depletion (1 ‰ to -10 ‰) in the latter part of the monsoon  
551 (Lekshmy et al., 2018; Rahul et al., 2016). The negative correlation found in this study, albeit minor, suggests  
552 that the ground-level vapour gets a significant contribution from drop evaporation. How can moisture generated  
553 by drop evaporation during raindrop descent contribute to the ground-level vapour? This is possible when there  
554 is a strong downdraft associated with intense monsoon rains (Risi et al., 2023). In a modelling study, Mandke et  
555 al. (1999) pointed out that deep convective cloud systems contain both upward and downward components. The  
556 downward motion is driven by the evaporation of falling precipitation and the dragging of the ambient air and  
557 vapour by big droplets. This downdraft brings moisture down from above and increases the vapour d-excess at  
558 the surface (Risi et al., 2010; Kurita, 2013; Aemisegger et al., 2015).

559 The existence of drop evaporation is further supported by a relation between  $\Delta d\text{-excess}_{r-v}$  and surface  
560 RH ( $R^2=0.31$ ; Fig. 6c). The difference between rain and vapour isotopes is higher (more negative) in lower RH  
561 and less in higher RH (Stewart, 1975). A similar analysis (Xing et al., 2023) in China also found that the change  
562 in isotopic composition is large when RH is less than 60 %.

563



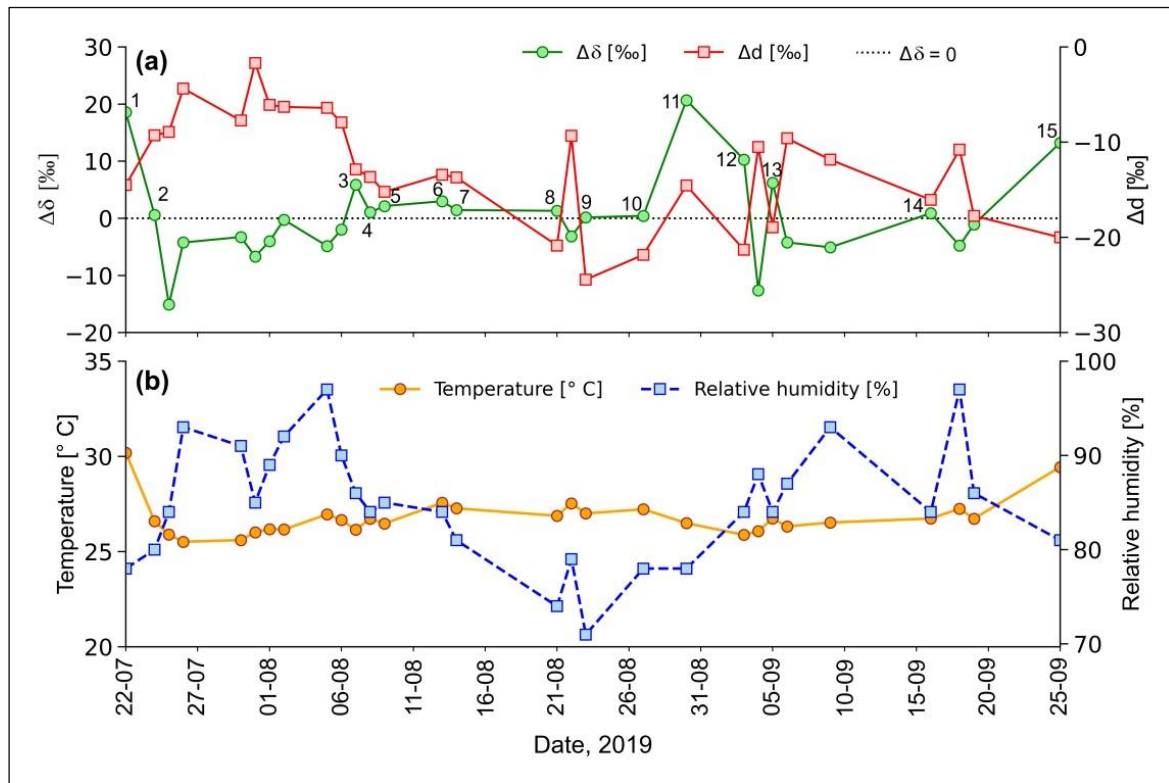
564

565 **Figure 6.** The correlations between (a)  $\delta^{18}\text{O}$  of rain ( $\delta^{18}\text{O}_r$ ) and  $\delta^{18}\text{O}$  of vapour ( $\delta^{18}\text{O}_v$ ) at the ground level; (b) the difference  
 566 in d-excess of rain and vapour ( $\Delta d\text{-excess}_{r-v}$ ) and  $\delta^{18}\text{O}$  ( $\Delta\delta^{18}\text{O}_{r-v}$ ) showing that the rain value is lower in d-excess whereas it  
 567 is higher in  $\delta^{18}\text{O}$ ; (c) difference in the d-excess of rain and vapour ( $\Delta d\text{-excess}_{r-v}$ ) and surface RH.

568

569 Falling raindrops and the vapour in the atmospheric column constitute an interacting two-phase system.  
 570 Below the cloud base, the water molecules are constantly exchanged between these two phases depending on the  
 571 ambient RH and T. The difference between isotopes ( $\delta D_v$  and  $d\text{-excess}_v$ ) of vapour in equilibrium with

572 raindrops and the observed surface vapour ( $\Delta\delta$  and  $\Delta d$ , respectively) is a useful signature of departure from  
 573 equilibrium exchange. Graf et al. (2019) demonstrated how the  $\Delta\delta$ - $\Delta d$  plot represents the effect of sub-cloud  
 574 processes, such as evaporation and equilibration, which influence the rain isotopes. The time series of  $\Delta\delta$  values  
 575 (Fig. 7a) for the Pune rain samples shows that the values varied between -15 ‰ and 21 ‰. For  $\Delta d$ , the time  
 576 series shows negative values in all cases (ranging from -2 ‰ to -24 ‰). The close-to-equilibrium samples  
 577 correspond mostly to the high-humidity period in July (Fig. 7b). Fifteen samples show the influence of below-  
 578 cloud evaporation with positive  $\Delta\delta$  values and associated strongly negative  $\Delta d$  values (up to -20 ‰).  
 579

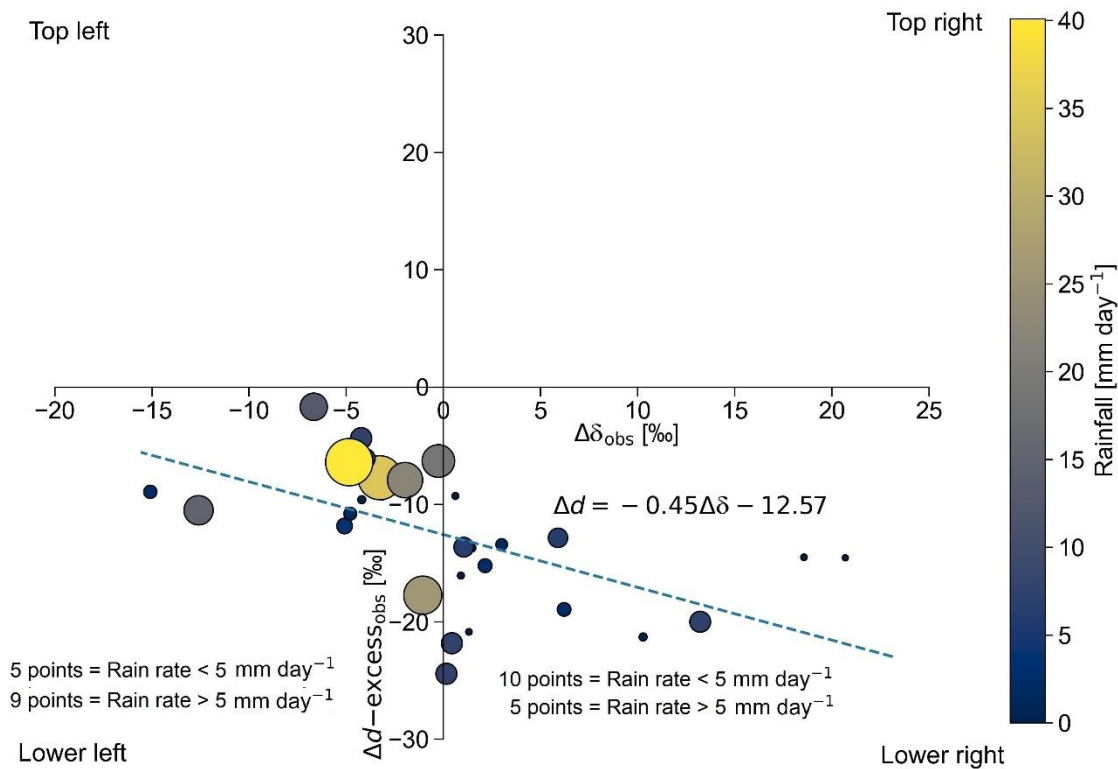


580  
 581 **Figure 7.** (a) Time series of  $\Delta\delta$  and  $\Delta d$  of the rain samples collected during 2019 monsoon (July to September) in Pune.  $\Delta\delta$   
 582 and  $\Delta d$  values (total points=29) denote rain-equilibrated vapour isotope minus the surface vapour isotope. The blue dotted  
 583 line indicates  $\Delta\delta=0$ . All data points where  $\Delta\delta>0$  are marked with numbers totalling 15. (b) Time series of daily average  
 584 surface T and RH recorded at the IMD observatory at Pune.

585  
 586 A  $\Delta\delta$ - $\Delta d$  scatter plot (Fig. 8) shows that none of the rain samples is in equilibrium with the  
 587 corresponding ground-level vapour. If the equilibrium pertained, the corresponding point would plot at the  
 588 origin. Fifteen points fall in the lower right quadrant of the diagram (positive  $\Delta\delta$  and negative  $\Delta d$  values), where  
 589 the raindrop evaporation is relatively more significant. The rainfall amount for these samples was low (less than  
 590  $5 \text{ mm day}^{-1}$ ), consistent with a substantial evaporation effect. Fourteen samples have both negative  $\Delta\delta$  and  $\Delta d$   
 591 values (located in the lower left quadrant), indicating incomplete equilibration with near-surface vapour. The  
 592 crucial driving factors for below-cloud processes seem to be the size of raindrops related to the intensity of  
 593 precipitation. This is because raindrops with larger diameters correspond to increased intensity and have shorter  
 594 residence times in the atmospheric column. As a result, they experience reduced evaporation during descent. It  
 595 is to be noted that the drop diameter in this study was not measured by a disdrometer directly. They were

596 estimated from the rain rate using the Marshall-Palmer relationship. Therefore, larger rain rates will always  
 597 translate to larger droplet sizes. This physical relationship is thought to be a result of increased collision-  
 598 coalescence during higher rainfall intensity (Law et al., 2021).

599 Distribution of points in the  $\Delta\delta$ - $\Delta d$  plot (Fig. 8) shows that 10 samples with  $<5 \text{ mm day}^{-1}$  rain rate fall  
 600 in the lower right quadrant compared to 5 samples in the left quadrant. This suggests that drop evaporation is a  
 601 dominant process in low rainfall events (where smaller drop diameters dominate). In Fig.8, the size and colour  
 602 of the points denote drop size and rainfall, respectively. It seems that larger drop size points with higher rainfall  
 603 plot in the lower left quadrant. This indicates that for larger sizes, the memory of the isotopes is partly retained  
 604 even after the sub-cloud evaporation. Twenty-nine samples are nearly equally distributed in the two quadrants,  
 605 suggesting an equal number of equilibration-dominant and evaporation-dominant rain events. It is to be noted  
 606 that deep convective rains during the monsoon exhibit significantly higher mass-weighted diameter compared to  
 607 shallow convective rains or stratiform rains (Kumar et al., 2025). The five big diameter points in the lower left  
 608 quadrant correspond to cases of deep convection.  
 609



610  
 611 **Figure 8.** The  $\Delta\delta$ - $\Delta d$  plot based on observed values for various rain rates. The size of the sample circles indicates drop size;  
 612 their variation is also associated with the rain rate (scale on right). We note that most of the (lower left) points are of a bigger  
 613 size, and those in the (lower right) are of a small size. The line shows a good fit to the data with a slope of -0.45.  
 614

615 The regression line in the  $\Delta\delta$ - $\Delta d$  cross plot (Fig. 8) has a slope of -0.45 based on Bootstrap analysis  
 616 (See SI-13). In contrast, Graf et al. (2019) obtained a smaller value of -0.30 for their study area, Zurich,  
 617 Switzerland. The difference is intriguing and merits a discussion. Their study was based on short-time intra-  
 618 event samples (covering about 16 hours and each rain sample being collected for 10 to 15 min) in a mid-latitude

619 region, whereas Pune samples were 29 daily rain collections in a tropical region (covering a few months and  
620 each collected for 24 hours). A set of complex processes operates to dictate the value of the slope, and Graf et  
621 al. (2019) pointed out that the slope could represent a balance between below-cloud evaporation and  
622 equilibration. They suggested that it would be insightful to explore the slope for other climatic regions, hinting  
623 that the slope will help assess the evaporation. A quantitative estimate of the evaporation fraction can be  
624 obtained from BCIM by using the mass loss parameter in the output (see section 4.3).

625 At higher humidity, the evaporation is lower, the change of  $\Delta d$  is smaller, and this leads to a lower  
626 slope. Conversely, when the temperature is higher, the slope is higher due to higher evaporation. The value of  
627 the slope is determined by a differential effect in evaporative fractionation. Evaporation decreases  $d_r$ , and  
628 increases  $\delta D_r$ , but the magnitudes of these changes (negative for  $d_r$  and positive for  $\delta D_r$ ) are not the same.  
629 Fractionation values (involving equilibrium and kinetic effects) show that the change in  $\delta D$  is larger compared  
630 to that in  $d$ -excess (about 30% of the  $\delta D$  change, considering the absolute values). This is because in  
631 evaporation, the kinetic fractionation occurs along with equilibrium fractionation, and the former has more  
632 influence on  $\delta D$  compared to  $\delta^{18}\text{O}$ . If evaporation is higher (due to higher  $T$  and lower  $\text{RH}$ ), the deviation of the  
633 predicted rain isotope values from those predicted by the equilibrium fractionation alone will be more, and the  
634 slope will be higher. In the frontal systems of Switzerland, the  $T$  was about  $12^\circ\text{C}$  and  $\text{RH}$  about 80 % (Graf et  
635 al., 2019), whereas in Pune, the  $T$  was about  $25^\circ\text{C}$  and  $\text{RH}$  about 85 %. Even though the  $\text{RH}$  was nearly similar,  
636 the  $T$  was much higher in Pune. This resulted in a higher slope for Pune (see next section).

637

#### 638 **4.3 Estimate of raindrop evaporation**

639 The output of BCIM in Run-3 predicts that the mass of the drop reduces as it falls. The ratio of final  
640 mass to the initial mass ( $m/m_0$ ) can then be used to estimate the fractional mass loss suffered by the drop on its  
641 way down. The difference  $(1-m/m_0)$  represents the effective rain evaporation. With this definition, a time series  
642 of evaporation values (Fig. 9a) shows variation from 4 % to 61 %. The average evaporation is 23 % if we  
643 consider all 29 values. But there are four large values 45, 47, 58 and 61%, all of which correspond to low  
644 rainfall or small drop diameter (Fig. 9d). If we exclude them, the average is 18 % ( $n=25$ ). As expected, drop  
645 evaporation is inversely related to relative humidity (Fig. 9b) and drop diameter (Fig. 9d) but directly  
646 proportional to the temperature (Fig. 9c). The relative importance of the three determining factors, namely,  $\text{RH}$ ,  
647  $T$  and drop diameter, is seen through the multiple regression equation of evaporation fraction. Here, we should  
648 use normalized multiple regression because simple (or unnormalized) multiple regression uses variables in their  
649 original units, while normalized multiple regression transforms all features onto a similar scale, allowing for  
650 direct comparison of feature importance. The normalized evaporation fraction as a function of normalized  
651 values of  $\text{RH}$ ,  $T$  and  $D$  shows that (1)  $D$  is the major determinant and (2)  $T$  plays an important role, nearly as  
652 much as  $\text{RH}$ , for evaporation.

653

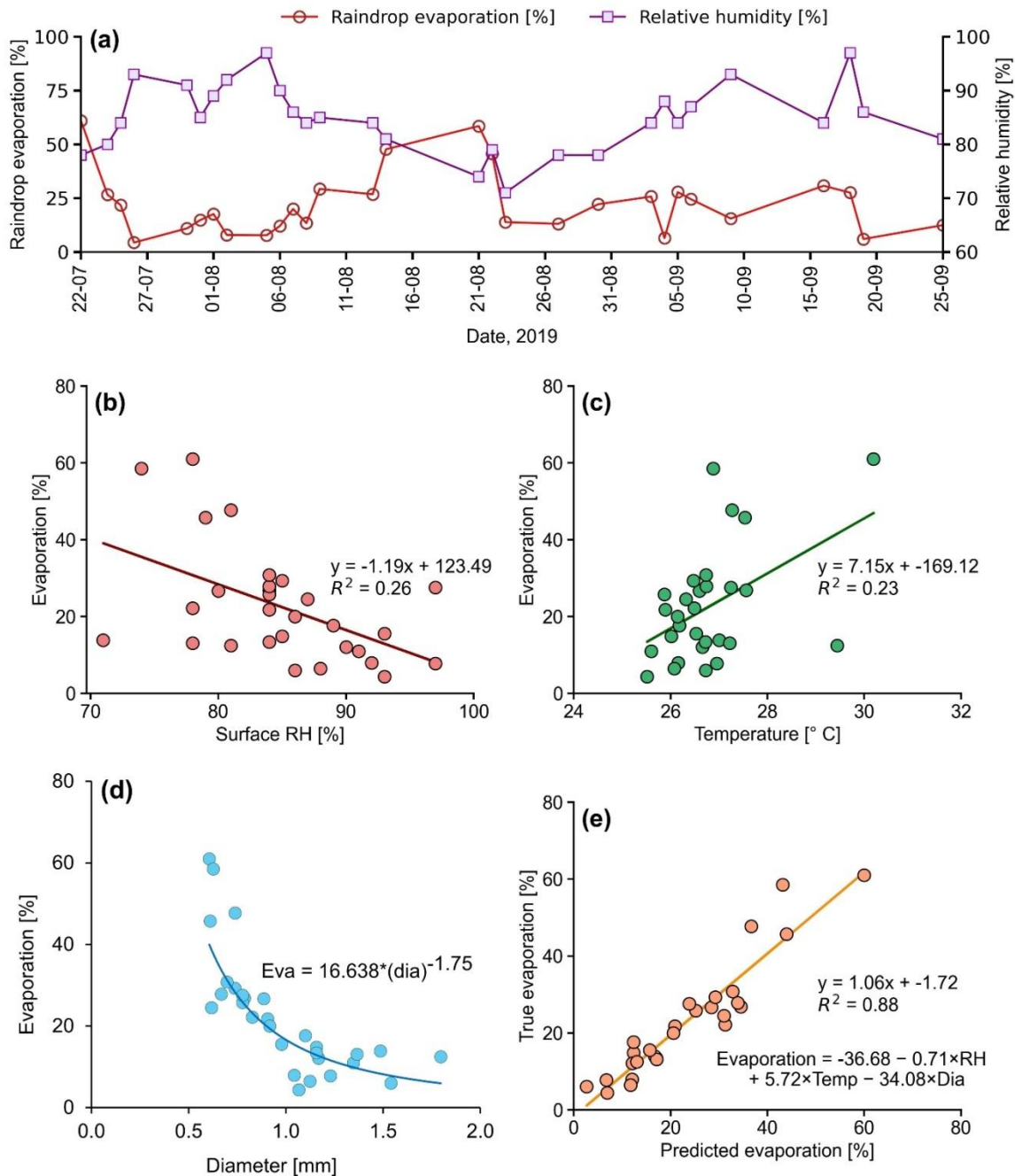
$$654 \text{ Normalized Evaporation Fraction} = -0.329* \text{RH} + 0.370* T - 0.665* \text{Diameter} \quad (2)$$

655

656 For the larger values of Pune temperatures, we expect more evaporation, and this leads to the higher slope value  
657 of -0.45 (in the  $\Delta\delta$ - $\Delta d$  cross plot) for Pune compared to -0.30 for Zurich, as noted in the previous section.

658

659 The evaporation was particularly high (61 % and 59 %) on 22 July and 21 August due to combined  
 660 effect of low RH (78 % and 74 %), and high T (30 °C and 27 °C) and small D (Fig. 9a). On average, the  
 661 evaporation fractions are moderately high (23±16) % consistent with the observed anti-correlation between  $d_r$   
 662 and  $\delta^{18}O_r$  of rain samples (Fig. 4b).  
 663



664  
 665 **Figure 9.** (a) Time series of raindrop evaporation using BCIM simulation (Run-3) and surface relative humidity. The  
 666 regression between raindrop evaporation fraction with (b) RH, (c) temperature, and (d) drop diameter. (e) Multiple  
 667 regression analysis yields the equation shown in the inset. The regression equation prediction of evaporation explains nearly  
 668 88% of the variance.

669  
 670

671 **4.4 The uncertainty in the evaporation fraction**

672 Among the controlling factors for evaporation, the temperature does not vary much (26.8±1.0 °C) or  
673 about 4%, while for RH, the variation (see SI-14) is slightly larger (85±6 %) or 7%. The diameter variation, on  
674 the contrary, is much higher, about 30% (1.0±0.3 mm) and has a higher impact on the evaporation. The net  
675 uncertainty in the evaporation fraction due to combined uncertainties in RH, T and D can be determined by a  
676 simple multiple regression equation (using unnormalized variables) as given below. The Evaporation Fraction  
677 (EF) was regressed with RH (in %), T (in °C) and the D (in mm). and yields:

678  
679 Evap. Fraction= -36.68 - 0.71\*RH + 5.72\*T - 34.08\*D (3)

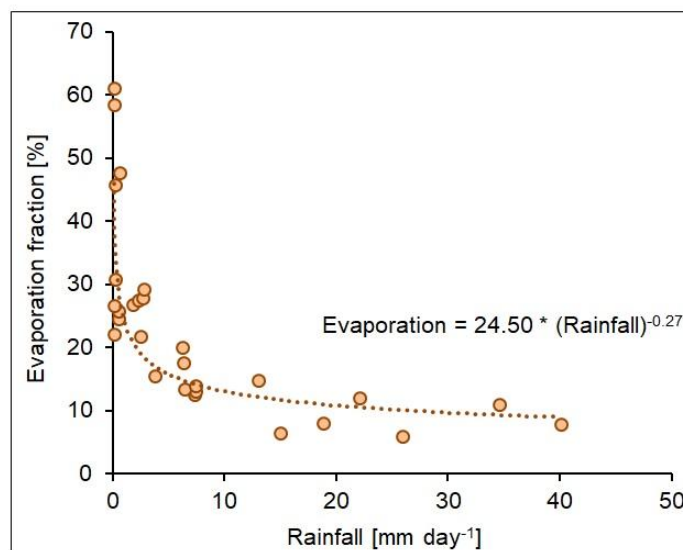
680  
681 The equation (3) can be used to estimate the error in drop evaporation, knowing the uncertainties in RH, T and  
682 D and using the partial regression coefficients as partial derivatives. Using the standard quadratic formula for  
683 error (Farrance and Frenkel, 2012), we write:

684  
685  $\sigma(EF)^2 = (\partial EF / \partial RH)^2 * \sigma(RH)^2 + (\partial EF / \partial T)^2 * \sigma(T)^2 + (\partial EF / \partial D)^2 * \sigma(D)^2$  (4)  
686

687 Where  $\sigma$  denotes the uncertainties in EF, RH, T and D, and the quantities in brackets express the partial  
688 derivative of EF with respect to the variable. The uncertainties associated with RH (see SI-14), T and D are  
689 discussed in section SI-10. Adding these three errors by the above quadratic formula, we obtain the error in the  
690 evaporation fraction for 29 days, which varies from 7.4 % to 13.8 % (for EF values from about 4 to 61 %). The  
691 average for 29 days is ±8.9 %, which is taken as the overall error in the evaporation estimate.

692  
693 **4.5 Evaporation and rainfall relation**

694 Evaporation fraction plotted as a function of rainfall (Fig. 10) shows a power law. For a smaller rainfall  
695 range (less than 5 mm day<sup>-1</sup>), evaporation affects the rainfall significantly. The reason is that smaller rainfall is  
696 usually associated with smaller drops, which are very sensitive to evaporation, resulting in a power law. If the  
697 EF increases by 10 % (say from 15 % to 25 %), the rainfall reduces by about 4 mm day<sup>-1</sup> (from 5 to 1 mm day<sup>-1</sup>).  
698



699

700 **Figure 10.** A scatter plot shows the relationship between the estimated raindrop evaporation and rainfall in Pune. The brown  
701 dotted line indicates the best-fit power law. Higher rainfall implies drops of a bigger size and hence a lower evaporation  
702 fraction.

703

704 It is instructive to compare our results to the evaporation estimates obtained in similar studies carried  
705 out in other climatic regimes. Using a steady state one-dimensional model of rain in the North Atlantic Trade  
706 Wind region (Barbados), Sarkar et al. (2023) found a high value of 63 % ( $63 \pm 23$  %) for raindrop evaporation  
707 (using radar reflectivity data on rain evaporation flux), which is three times more than our average value of 23  
708 % ( $23 \pm 16$  %). The reason for the large difference in Pune evaporation from Barbados is possibly due to a large  
709 difference in drop diameter and RH. A comparison reveals that in Barbados, the drop diameter were much  
710 smaller (from 0.1 mm to 0.6 mm) in comparison to ours (from 0.606 mm to 1.796 mm). The Barbados drops  
711 were so small that in some cases (smaller than 0.3 mm on 4 February 2020), they evaporated completely  
712 (evaporation  $\sim 100\%$ ) during descent. In addition, in their sampling region, the RH was lower, ranging from 65  
713 % to 80 %, compared to ours (74 % to 97 %). A smaller drop diameter and lower RH lead to higher raindrop  
714 evaporation. In contrast, only four high evaporation days (more than 45 %) occurred in Pune out of 29 sampling  
715 days. We also note that their drop diameters varied over a wider range, leading to a larger variability compared  
716 to our study.

717 In a similar study as here, rain and vapour isotopes were measured in a cold-front passage over Zurich  
718 during 19-25 July 2011, and the data were interpreted by an isotope-enabled regional weather prediction model  
719 COSMOiso (Aemisegger et al., 2015). The authors showed that by switching off the raindrop evaporation, the  
720 rainfall increased by about 75 % because the cooling induced by evaporation causes diminished convective  
721 activity. The estimated average evaporation in their study was about 40 %. This value is nearly twice our value.  
722 The reason is probably a smaller drop diameter and lower RH; The authors write: "weak rainfall intensities  
723 (small droplets and thus lower falling velocities), and possibly lower relative humidity in the air column could  
724 have contributed to the evaporative enrichment of precipitation".

725

#### 726 **4.6 Limitations and uncertainty of the derived parameters**

727 The isotope technique and the BCIM are associated with the following limitations:

728 (a) We used TES satellite data averaged over 2005-2009 to guide our choice of vapour isotope profiles, but the  
729 year of analysis was 2019. In this matter, there is no way to ascertain the degree of deviation of the true  
730 profiles from the adopted ones in Run-3.

731 (b) There are limitations on the use of RH and T from radiosonde. The mean radiosonde data for Pune are  
732 expected to be reasonable if we can show that the difference between the two consecutive measurements is  
733 not large. Radiosondes are launched to measure at 00 Z and 12 Z and are generally not carried out when  
734 there is rain. We determined that two soundings taken on the same day are similar to within 8 % RH and 1  
735 °C on most days. Analysis of radiosonde daily variability can be found in the (SI-14). We also show  
736 through sensitivity analyses and multiple regression analyses that the effects of the daily scale variation in  
737 RH and T on model rain isotope values and evaporation fraction are not significant. We demonstrate further  
738 that the RH and T data from the radiosonde is more reliable than the same obtained from any satellite  
739 datasets. The  $\delta^{18}\text{O}_v$  profiles were adopted based on the  $\delta D_v$  and  $\delta^{18}\text{O}_v$  profiles obtained from the LMDZ

740 model. Run-3 uses radiosonde for the thermodynamic profile,  $\delta D_v$  from satellite data from 2005-2009, and  
741  $\delta^{18}O_v$  from the  $d_v$  of the LMDZ extrapolated to the observed vapour measurement at the ground. We realize  
742 that there are major concerns with these inputs coming from different data products that all have different  
743 spatial/temporal scales and measurement principles. But we note that when any atmospheric model is  
744 initialized, the input parameters from various sources are used, which may have different spatial and  
745 temporal resolutions and measurement principles. Moreover, datasets from various sources are also utilized  
746 in atmospheric models across different parametrization schemes and nudging. In support of isotope tuning,  
747 we note that nudging is a well-known technique where the model values are adjusted to accord with the  
748 observed values. For example, Graf et al. (2019) used point-based radiosonde RH and T observations, as  
749 well as isotope outputs from a limited-area model (Pfahl et al., 2012; Villiger et al., 2023), with a km-scale  
750 resolution. These two datasets have different scales and measurement principles. Guided by their argument,  
751 we have taken the average radiosonde profiles of each sampling day as our choice and adjusted the  
752 lowermost parts to match the measured RH and T values at the ground taken from the IMD.

753 (c) The isotope profiles were constructed initially using ground observations as boundary values. However, this  
754 resulted in a mismatch with the observed values in Run-2, and we had to tune to lower  $\delta D_v$  values and  
755 higher  $\delta^{18}O_v$  values (and consequently lower  $d_v$  values) to achieve good agreement. It should be mentioned  
756 here that Risi et al. (2023) discussed a similar idea in their study of water isotopes in tropical squall lines;  
757 they indicated that convective downdrafts can introduce depleted vapour produced by rain re-evaporation in  
758 the boundary layer. Another limitation is that the vapour samples were collected for a duration of about a  
759 few hours, which did not coincide exactly with the 24-h rain collection period.

760 (d) The raindrop formation height was assumed to be the CLWC peak level for all rainy days, and the drops  
761 were all introduced at that level. However, it is well known that raindrops do not all form at the same  
762 height, even on a single day. With the single height assumption for drop introduction, we are neglecting  
763 alterations in isotope ratios produced inside the cloud by various microphysical processes.

764 (e) Although some studies pointed out that collision-coalescence is an important warm rain process that occurs  
765 in the WG regions of India (Konwar et al., 2014), we did not include it in the model. Since the BCIM  
766 follows the evolution of a single droplet, there is no opportunity for collision coalescence, and we have to  
767 rely on the input droplet diameter being representative of droplet sizes that would occur through collision-  
768 coalescence processes. In theory, this is all built into the Marshall-Palmer relationship.

769 (f) The uncertainty values for  $\delta D_r$  is 3.5 %, for  $d_r$  it is 1.7 %, and for drop evaporation it is 8.9 %.  
770 Several assumptions are required to calculate the uncertainties in these parameters (details are given in the  
771 SI-10 and SI-11), and some of them (like the linear dependence assumption in multiple regression) may be  
772 open to questions.

773

#### 774 **4.7 Impact of evaporation on rainfall and heat budget**

775 Presence of evaporation of raindrops during the ISM has been postulated earlier in several theoretical  
776 models, but this study provides, for the first time, a quantitative estimate of rain evaporation on a day-to-day  
777 basis in the monsoon season using combined rain and vapour isotope data in a BCIM. We found that about 23 %  
778 raindrop evaporation occurred in the 2019 monsoon season in the highly humid Pune region. The average  
779 seasonal rainfall in Pune is about 55 cm (during monsoon), and if ~23 % of this is evaporated, it would mean

780 considerable cooling of the boundary layer, leading to localized downdrafts, formation of cold pools, and  
781 changes in atmospheric stability. Cooling can also hinder efficient formation of convection (Hwong and Muller,  
782 2024) and can have a large effect on the precipitation patterns in the tropics (Bacmeister et al., 2006; Sarkar et  
783 al., 2023). Given the large share of precipitation recycling found in this study for Pune, the question arises as to how  
784 large the precipitation recycling is at regional or continental scales. We need to have a comprehensive program for  
785 carrying out such analysis, aided with appropriate BCIM input parameters, to understand the evaporation of  
786 raindrops over various climatic subdivisions in India. Moreover, high-frequency observations of vapour and rain  
787 isotopes would be useful to quantify this fraction during various convective events associated with low-pressure  
788 systems during the monsoon. A quantitative estimate of raindrop evaporation would be highly useful for  
789 modelling the energy and moisture budgets during the monsoon season.

790

## 791 5. Conclusions

- 792 (1) This study reveals substantial temporal variability in atmospheric vapour isotopes in Pune during the  
793 2019 monsoon, with  $\delta^{18}\text{O}_v$  ranging from  $-19.2\text{‰}$  to  $-9.4\text{‰}$  and  $\delta\text{D}_v$  from  $-123.7\text{‰}$  to  $-63.4\text{‰}$ . Rain  
794 isotopes show comparatively smaller variability ( $\delta^{18}\text{O}_r$ :  $-7.5\text{‰}$  to  $1.2\text{‰}$ ;  $\delta\text{D}_r$ :  $-58.9\text{‰}$  to  $11.8\text{‰}$ ).
- 795 (2) Four events of markedly depleted rain and vapour isotopes were identified, coinciding with negative  
796 OLR anomalies and high rainfall indicative of strong convection and the effect of Rayleigh  
797 condensation. These events likely reflect the uplift of moist air parcels to higher altitudes ( $\sim 5.5\text{ km}$ ) and  
798 condensation to droplets during ascent following Rayleigh distillation.
- 799 (3) Vapour isotope data show a distinct seasonal trend, with increasing vapour  $d_v$  and slightly decreasing  
800  $\delta^{18}\text{O}_v$  after mid-August, particularly in September. The strong anti-correlation between vapour  $\delta^{18}\text{O}_v$   
801 and  $d_v$  at the ground suggests increasing contributions from evaporative sources over time.  
802 Downdrafted vapour with potential contribution from raindrop evaporation possibly constitutes one  
803 such source.
- 804 (4)  $\Delta\delta$ - $\Delta d$  analysis further confirms the importance of sub-cloud evaporation, with  $\sim 50\%$  of data points  
805 falling in the evaporation-dominated quadrant. The derived slope ( $-0.45$ ) indicates stronger  
806 evaporation compared to mid-latitude systems, consistent with higher temperatures ( $\sim 25\text{ °C}$ ) in Pune,  
807 enhancing kinetic fractionation effects.
- 808 (5) To quantify the sub-cloud processes altering the rain isotope values, we used the BCIM. Upon  
809 reasonable tuning of the input parameters, we obtained good agreement between the observed and  
810 model rain isotope values at the ground level. Using the model, raindrop evaporation is quantified on a  
811 daily scale, revealing an average mass loss of  $\sim 23\%$  (range:  $4\% - 61\%$ ) in the sub-cloud layer.  
812 Excluding the extreme cases, evaporation averages  $18 \pm 8\%$ , highlighting substantial modification of  
813 rain isotopes.
- 814 (6) Raindrop evaporation can reduce the rainfall substantially, especially during low rain (less than  $10\text{ mm}$   
815  $\text{day}^{-1}$ ). The average seasonal evaporation means considerable cooling of the boundary layer, leading to  
816 localized downdrafts, formation of cold pools, and changes in atmospheric stability hindering efficient  
817 formation of convection.

818

819

820 **Data Availability**

821 Observed rain and vapour isotope data are available upon communication with the corresponding author. The  
822 upper-air radiosonde measurements were obtained from the University of Wyoming repository  
823 (<http://weather.uwyo.edu/upperair/sounding.html>). The daily gridded data (zonal and meridional wind, specific  
824 humidity, air temperature, and cloud liquid water content) are available from the European Centre for Medium-  
825 Range Weather Forecasts Reanalysis (ERA-5; [https://www.ecmwf.int/en/forecasts/datasets/reanalysis-](https://www.ecmwf.int/en/forecasts/datasets/reanalysis-datasets/era5)  
826 [datasets/era5](https://www.ecmwf.int/en/forecasts/datasets/reanalysis-datasets/era5)). The rainfall data (cumulated over 24 hours) are obtained from the Pune observatories of the IMD  
827 (available at the National Data Centre ([www.imdpune.gov.in/ndc\\_new/ndc\\_index.html](http://www.imdpune.gov.in/ndc_new/ndc_index.html))). Apart from daily  
828 rainfall, hourly rainfall data and daily average temperature and relative humidity data for the Pune observatory  
829 were also obtained from the IMD using the above link. The datasets for 48 h air mass back trajectory analysis at  
830 850 mb pressure level are obtained from the NOAA Hybrid Single-Particle Lagrangian Integrated Trajectory  
831 (HYSPLIT) model (<https://www.ready.noaa.gov/HYSPLIT.php>). We received daily outputs of LMDZ isotope-  
832 enabled GCMs, which were provided by Dr. Camille Risi by personal communication. The Interpolated  
833 Outgoing Longwave Radiation (OLR) data from NOAA  
834 (<https://psl.noaa.gov/data/gridded/data.olrcdr.interp.html>) is used in this study. Tropospheric Emission  
835 Spectrometer (TES) Level 2 (Nadir-Lite-Version 6) retrievals of HDO and H<sub>2</sub>O profiles for the available period  
836 (2005–2007; <https://tes.jpl.nasa.gov/tes/data>) are used to construct the vapour  $\delta D$  profile.

837  
838 **Author Contribution**

839  
840 SSN carried out all rain and vapour isotopic measurements and part of the data analyses, installed and ran the  
841 model BCIM. SPR analyzed most of the samples to get the isotopic data, performed all controlled runs in the  
842 BCIM, and constructed most of the figures. SS conceptualized the scientific plan and methodology and wrote  
843 the initial draft of the manuscript. SKB contributed to data analysis and interpretation of model outputs,  
844 corrected the manuscript, and provided useful comments and suggestions. NA contributed to data analysis and  
845 simulation.

846  
847 **Code Availability**

848 We carried out data analysis and plots using licensed versions of Microsoft Excel and Python, the latter being  
849 freely available from <https://www.python.org/downloads/>. The code of the model, BCIM, is freely available  
850 from <https://git.app.uib.no/Harald.Sodemann/bcim>.

851  
852 **Competing interests**

853 The authors declare that they have no conflict of interest.

854  
855 **Acknowledgements**

856 The Indian Institute of Tropical Meteorology, Pune (IITM), is fully supported by the Earth System Science  
857 Organization (ESSO) of the Ministry of Earth Sciences, India. This work forms part of the Ph.D. thesis of SSN,  
858 who thanks IITM for a fellowship. SPR thanks IITM for a research associateship. We thank Director IITM for  
859 his constant encouragement. The NASA Langley Research Centre and the Atmospheric Science Data Centre are  
860 acknowledged for the TES dataset. A fruitful discussion with Dr. Camille Risi is also acknowledged. We thank

861 Dr. Pallab Roy for helping with the Bootstrap analysis and making several plots. Dr. Rohit Pradhan of Space  
862 Application Centre is acknowledged for processing the TES dataset.

863

## 864 **References**

865 Aemisegger, F., Spiegel, J. K., Pfahl, S., Sodemann, H., Eugster, W., and Wernli, H.: Isotope meteorology of  
866 cold front passages: A case study combining observations and modeling, *Geophys. Res. Lett.*, 42, 5652–5660,  
867 <https://doi.org/10.1002/2015GL063988>, 2015.

868 Bacmeister, J. T., Suarez, M. J., and Robertson, F. R.: Rain re-evaporation, boundary layer–convection  
869 interactions, and Pacific rainfall patterns in an AGCM, *J. Atmos. Sci.*, 63, 3383–3403,  
870 <https://doi.org/10.1175/JAS3791.1>, 2006.

871

872 Bhattacharya, S. K., Froehlich, K., Aggarwal, P. K., and Kulkarni, K. M.: Isotopic variation in Indian Monsoon  
873 precipitation: Records from Bombay and New Delhi, *Geophys. Res. Lett.*, 30(24), 2285,  
874 <https://doi.org/10.1029/2003GL018453>, 2003.

875

876 Bonne, J. L., Masson-Delmotte, V., Cattani, O., Delmotte, M., Risi, C., Sodemann, H., and Steen-Larsen, H. C.:  
877 The isotopic composition of water vapour and precipitation in Ivittuut, southern Greenland, *Atmos. Chem.*  
878 *Phys.*, 14, 4419–4439, <https://doi.org/10.5194/acp-14-4419-2014>, 2014.

879 Brubaker, K. L., Entekhabi, D., and Eagleson, P. S.: Estimation of Continental Precipitation Recycling, *J.*  
880 *Climate*, 6, 1077–1089, [https://doi.org/10.1175/1520-0442\(1993\)006<1077:EOCPR>2.0.CO;2](https://doi.org/10.1175/1520-0442(1993)006<1077:EOCPR>2.0.CO;2), 1993.

881 Chakraborty, S., Sinha, N., Chattopadhyay, R., Sengupta, S., Mohan, P. M., and Datye, A.: Atmospheric  
882 controls on the precipitation isotopes over the Andaman Islands, Bay of Bengal, *Sci. Rep.*, 6, 19555,  
883 <https://doi.org/10.1038/srep19555>, 2016.

884 Crawford, J., Hollins, S. E., Meredith, K. T., and Hughes, C. E.: Precipitation stable isotope variability and  
885 subcloud evaporation processes in a semi-arid region, *Hydrol. Process.*, 31, 20–34,  
886 <https://doi.org/10.1002/hyp.10885>, 2017.

887 Dansgaard, W.: Stable isotopes in precipitation, *Tellus A: Dynamic Meteorology and Oceanography*, 16, 436,  
888 <https://doi.org/10.3402/tellusa.v16i4.8993>, 2012.

889 Deshpande, R. D., Maurya, A. S., Kumar, B., Sarkar, A., and Gupta, S. K.: Rain-vapor interaction and vapor  
890 source identification using stable isotopes from semiarid western India, *J. Geophys. Res.*, 115, 2010JD014458,  
891 <https://doi.org/10.1029/2010JD014458>, 2010.

892 Draxler, R. R., and Hess, G.: Description of the HYSPLIT4 modeling system, 1997.

893 Foote, G. B., and du Toit, P. S.: Terminal Velocity of Raindrops Aloft, *J. App. Meteorol. (1962-1982)*, 8, 249–  
894 253, 1969.

895 Farrance, I., and Frenkel, R.: Uncertainty of Measurement: A Review of the Rules for Calculating Uncertainty  
896 Components through Functional Relationships, *Clin. Biochem. Rev.*, 33(2), 49–75, 2012.

897

898 Froehlich, K., Kralik, M., Papesch, W., Rank, D., Scheifinger, H., and Stichler, W.: Deuterium excess in  
899 precipitation of Alpine regions – moisture recycling, *Isot. Environ. Health Stud.*, 44, 61–70,  
900 <https://doi.org/10.1080/10256010801887208>, 2008.

901 Gat, J. R.: Oxygen and hydrogen isotopes in the hydrologic cycle, *Annu. Rev. Earth Planet. Sci.*, 24, 225–262,  
902 <https://doi.org/10.1146/annurev.earth.24.1.225>, 1996.

903 Graf, P., Wernli, H., Pfahl, S., and Sodemann, H.: A new interpretative framework for below-cloud effects on  
904 stable water isotopes in vapour and rain, *Atmos. Chem. Phys.*, 19, 747–765, [https://doi.org/10.5194/acp-19-747-](https://doi.org/10.5194/acp-19-747-2019)  
905 2019, 2019.

906 Gray, W. M.: Fundamental importance of convective downdrafts and mass recycling within the tropical cloud

907 cluster and the Typhoon-Hurricane, *Trop. Cyclone Res. and Rev.*, 1, 130–141,  
908 <https://doi.org/10.6057/2012TCRR01.14>, 2012.

909 Herman, R. L., Cherry, J. E., Young, J., Welker, J. M., Noone, D., Kulawik, S. S., and Worden, J.: Aircraft  
910 validation of Aura Tropospheric Emission Spectrometer retrievals of HDO / H<sub>2</sub>O, *Atmos. Meas. Tech.*, 7, 3127–  
911 3138, <https://doi.org/10.5194/amt-7-3127-2014>, 2014.

912 Hersbach, H., Bell, B., Berrisford, P., Hirahara, S., Horányi, A., Muñoz-Sabater, J., Nicolas, J., Peubey, C.,  
913 Radu, R., Schepers, D., Simmons, A., Soci, C., Abdalla, S., Abellan, X., Balsamo, G., Bechtold, P., Biavati, G.,  
914 Bidlot, J., Bonavita, M., De Chiara, G., Dahlgren, P., Dee, D., Diamantakis, M., Dragani, R., Flemming, J.,  
915 Forbes, R., Fuentes, M., Geer, A., Haimberger, L., Healy, S., Hogan, R. J., Hólm, E., Janisková, M., Keeley, S.,  
916 Laloyaux, P., Lopez, P., Lupu, C., Radnoti, G., De Rosnay, P., Rozum, I., Vamborg, F., Villaume, S., and  
917 Thépaut, J.: The ERA5 global reanalysis, *Quart. J. Royal Meteorol. Soc.*, 146, 1999–2049,  
918 <https://doi.org/10.1002/qj.3803>, 2020.

919 Hwong, Y. L., and Muller, C. J.: The unreasonable efficiency of total rain evaporation removal in triggering  
920 convective self-aggregation, *Geophys. Res. Lett.*, 51, p.e2023GL106523,  
921 <https://doi.org/10.1029/2023GL106523>, 2024.  
922

923 Ingleby, B., Pauley, P., Kats, A., Ator, J., Keyser, D., Doerenbecher, A., Fucile, E., Hasegawa, J., Toyoda, E.,  
924 Kleinert, T., Qu, W., St. James, J., Tennant, W., and Weedon, R.: Progress toward high-resolution, real-time  
925 radiosonde reports, *Bull. Amer. Meteor. Soc.*, 97(11), 2149–2161, [https://doi.org/10.1175/BAMS-D-15-](https://doi.org/10.1175/BAMS-D-15-00169.1)  
926 00169.1, 2016.  
927

928 IPCC, A.: Climate change 2014 synthesis report, IPCC: Geneva, Switzerland, 1059–1072, 2014.

929 Jensen, M. P., Holdridge, D. J., Survo, P., Lehtinen, R., Baxter, S., Toto, T., and Johnson, K. L.: Comparison of  
930 Vaisala radiosondes RS41 and RS92 at the ARM Southern Great Plains site, *Atmos. Meas. Tech.*, 9, 3115–  
931 3129, <https://doi.org/10.5194/amt-9-3115-2016>, 2016.

932 Jiang, Y., Yang, L., Li, J., Zeng, Y., Tong, Z., Li, X., and Li, H.: Diurnal variation characteristics of raindrop  
933 size distribution observed by a Parsivel<sup>2</sup> Disdrometer in the Ili River valley, *Adv. Meteorol.*, 481661,  
934 <https://doi.org/10.1155/2024/1481661>, 2024.  
935

936 Konwar, M., Das, S. K., Deshpande, S. M., Chakravarty, K., and Goswami, B. N.: Microphysics of clouds and  
937 rain over the Western Ghat, *J. Geophys. Res.-Atmos.*, 119, 6140–6159, <https://doi.org/10.1002/2014JD021606>,  
938 2014.

939 Kumar, S., Resmi, E. A., Jash, D., Patade, S., Sumesh, R.K., Andrews, A., Sukumar, N., Aswini, A.R., and  
940 Kulkarni, G.: Raindrop size distribution in stratiform precipitation: Insights from spectral bin simulations over  
941 the high-altitude cloud physics observatory, Western Ghats, *J. Atmos. Sol.-Terr. Phys.*, 277, 106643, 2025  
942

943 Kumar, S., Hazra, A., and Goswami, B. N.: Role of interaction between dynamics, thermodynamics and cloud  
944 microphysics on summer monsoon precipitating clouds over the Myanmar Coast and the Western Ghats, *Clim.*  
945 *Dynam.*, 43, 911–924, <https://doi.org/10.1007/s00382-013-1909-3>, 2014.

946 Kumar, T. V. L., Durga, G. P., Rao, K. K., Nagendra, H., and Mall, R. K.: Moisture recycling over the Indian  
947 monsoon core region in response to global warming from CMIP5 models, *Indian Summer Monsoon Variability,*  
948 *El-Nino Teleconnections and Beyond*, Elsevier, 449–466, [https://doi.org/10.1016/B978-0-12-822402-1.00008-](https://doi.org/10.1016/B978-0-12-822402-1.00008-9)  
949 9, 2021.

950 Kurita, N.: Water isotopic variability in response to mesoscale convective system over the tropical ocean, *J.*  
951 *Geophys. Res.-Atmos.*, 118, <https://doi.org/10.1002/jgrd.50754>, 2013.

952 Law, S. L. G., Kuok, K. K., and Trinidad, S. G.: An Experimental Study on The Correlation of Natural Rainfall  
953 Intensities and Raindrop Size Distribution Characteristics, 2021 IOP Conf. Ser.: Mater. Sci. Eng. 1101 012009,  
954 10.1088/1757-899X/1101/1/012009, 2021.  
955

956 Lee, C., Lawson, W. G., Richardson, M. I., Anderson, J. L., Collins, N., Hoar, T., and Mischna, M.:

- 957 Demonstration of ensemble data assimilation for Mars using DART, MarsWRF, and radiance observations from  
958 MGS TES, *J. Geophys. Res.*, 116, E11011, <https://doi.org/10.1029/2011JE003815>, 2011.
- 959 Lee, J., and Fung, I.: Amount effect of water isotopes and quantitative analysis of post-condensation processes,  
960 *Hydrol. Process.*, 22, 1–8, <https://doi.org/10.1002/hyp.6637>, 2008.
- 961 Lekshmy, P. R., Midhun, M., Ramesh, R., and Jani, R. A.:  $^{18}\text{O}$  depletion in monsoon rain relates to large-scale  
962 organized convection rather than the amount of rainfall, *Sci. Rep.*, 4, 5661, <https://doi.org/10.1038/srep05661>,  
963 2014.
- 964 Lekshmy, P. R., Midhun, M., and Ramesh, R.: Influence of stratiform clouds on  $\delta\text{D}$  and  $\delta^{18}\text{O}$  of monsoon water  
965 vapour and rain at two tropical coastal stations, *J. Hydrol.*, 563, 354–362,  
966 <https://doi.org/10.1016/j.jhydrol.2018.06.001>, 2018.
- 967 Li, X., Tang, C., and Cui, J.: Intra-Event Isotopic Changes in Water Vapor and Precipitation in South China,  
968 *Water*, 13, 940, <https://doi.org/10.3390/w13070940>, 2021.
- 969 Marshall, J. S., and Palmer, W. McK.: The distribution of raindrops with size, *J. Meteorol.*, Shorter  
970 contributions, 5, 165-166, 1948.
- 971  
972 Mandke, S. K., Soman, M. K., and Satyan, V.: Impact of convective downdrafts in a GCM on the simulated  
973 mean Indian Summer Monsoon and its variability, *J. Meteorol. Soc. Jpn*, 77, 1061–1082,  
974 [https://doi.org/10.2151/jmsj1965.77.5\\_1061](https://doi.org/10.2151/jmsj1965.77.5_1061), 1999.
- 975 Midhun, M., Lekshmy, P. R., Ramesh, R., Yoshimura, K., Sandeep, K. K., Kumar, S., Sinha, R., Singh, A., and  
976 Srivastava, S.: The effect of monsoon circulation on the stable isotopic composition of rainfall, *J. Geophys.*  
977 *Res.-Atmos.*, 123, 5205–5221, <https://doi.org/10.1029/2017JD027427>, 2018.
- 978 Moerman, J. W., Cobb, K. M., Adkins, J. F., Sodemann, H., Clark, B., and Tuen, A. A.: Diurnal to interannual  
979 rainfall  $\delta^{18}\text{O}$  variations in northern Borneo driven by regional hydrology, *Earth Planet. Sci. Lett.*, 369–370, 108–  
980 119, <https://doi.org/10.1016/j.epsl.2013.03.014>, 2013.
- 981 Morrison, H., van Lier-Walqui, M., Fridlind, A. M., Grabowski, W. W., Harrington, J. Y., Hoose, C., et al.:  
982 Confronting the challenge of modeling cloud and precipitation microphysics, *J. Adv. . Model. Earth Syst.*, 12,  
983 e2019MS001689, <https://doi.org/10.1029/2019MS001689>, 2020.
- 984  
985 Munksgaard, N. C., Zwart, C., Haig, J., Cernusak, L. A., and Bird, M. I.: Coupled rainfall and water vapour  
986 stable isotope time series reveal tropical atmospheric processes on multiple timescales, *Hydrol. Process.*, 34,  
987 111–124, <https://doi.org/10.1002/hyp.13576>, 2020.
- 988 Murali Krishna, U. V., Das, S. K., Sulochana, E. G., Bhowmik, U., Deshpande, S. M., and Pandithurai, G.:  
989 Statistical characteristics of raindrop size distribution over the Western Ghats of India: wet versus dry spells of  
990 the Indian summer monsoon, *Atmos. Chem. Phys.*, 21, 4741–4757, <https://doi.org/10.5194/acp-21-4741-2021>,  
991 2021.
- 992 Naik, M., Jadhav, A. V., Mukhim, S., Kumar, P. P., and Rohini, L.: Bhawar-Cloud base height variability  
993 observed using a Laser- Based Ceilometer over a tropical station Pune, India, *Int. J. Remote Sens.*, 45,  
994 <https://doi.org/10.1080/01431161.2024.2402003>, 2003.
- 995  
996 Nimya, S. S., Sengupta, S., Parekh, A., Bhattacharya, S. K., and Pradhan, R.: Region-specific performances of  
997 isotope enabled general circulation models for Indian summer monsoon and the factors controlling isotope  
998 biases, *Clim. Dynam.*, 59, 3599–3619, <https://doi.org/10.1007/s00382-022-06286-1>, 2022.
- 999  
1000 Noone D.: Pairing measurements of the water vapor isotope ratio with humidity to deduce atmospheric  
1001 moistening and dehydration in the tropical mid-troposphere, *J. Climate*, 25(13), 4476-4494,  
1002 <https://doi.org/10.1175/JCLI-D-11-00582.1>, 2012.
- 1003  
1004 Pathak, A., Ghosh, S., and Kumar, P.: Precipitation recycling in the Indian subcontinent during summer

- 1005 monsoon, *J. Hydrometeorol.*, 15, 2050–2066, <https://doi.org/10.1175/JHM-D-13-0172.1>, 2014.
- 1006 Pattanaik, D., Mandal, R., Dey, A., Phani, R., Chattopadhyay, R., Joseph, S., Sahai, A., and Mohapatra, M.:  
1007 Extended Range Forecast (ERF) During Southwest Monsoon 2019, 2019.
- 1008 Pfahl, S., Wernli, H., and Yoshimura, K.: The isotopic composition of precipitation from a winter storm – A  
1009 case study with the limited-area model COSMO<sub>iso</sub>, *Atmos. Chem. Phys.*, 12, 1629–1648,  
1010 <https://doi.org/10.5194/acp-12-1629-2012>, 2012.
- 1011 Pradhan, R., Singh, N., and Singh, R. P.: Onset of summer monsoon in Northeast India is preceded by enhanced  
1012 transpiration, *Sci. Rep.*, 9, 18646, <https://doi.org/10.1038/s41598-019-55186-8>, 2019.
- 1013 Pranindita, A., Wang-Erlandsson, L., Fetzer, I., and Teuling, A. J.: Moisture recycling and the potential role of  
1014 forests as moisture source during European heatwaves, *Clim. Dynam.*, 58, 609–624,  
1015 <https://doi.org/10.1007/s00382-021-05921-7>, 2022.
- 1016 Pruppacher, H., and Klett, J.: Microstructure of atmospheric clouds and precipitation, in: *Microphysics of clouds  
1017 and precipitation*, Atmospheric and Oceanographic Sciences Library, vol. 18, Springer Netherlands, Dordrecht,  
1018 10–73, [https://doi.org/10.1007/978-0-306-48100-0\\_2](https://doi.org/10.1007/978-0-306-48100-0_2), 2010.
- 1019 Rahul, P., Ghosh, P., Bhattacharya, S. K., and Yoshimura, K.: Controlling factors of rainwater and water vapor  
1020 isotopes at Bangalore, India: Constraints from observations in 2013 Indian monsoon, *J. Geophys. Res. Atmos.*,  
1021 121, <https://doi.org/10.1002/2016JD025352>, 2016.
- 1022 Rajaveni, S. P., Nimya, S. S., Sengupta, S., Datye, A., and Sarma, D.: Three years of stable water isotope data of  
1023 daily rain samples collected from three geomorphic regions of India, *Sci. Data*, 11, 1445,  
1024 <https://doi.org/10.1038/s41597-024-04308-7>, 2024.
- 1025 Rao, Y.P.: *Southwest Monsoon*, Meteorological Monograph Synoptic Meteorology No.1., India Meteorological  
1026 Department, 1976.
- 1027 Risi, C., Bony, S., and Vimeux, F.: Influence of convective processes on the isotopic composition ( $\delta^{18}\text{O}$  and  $\delta\text{D}$ )  
1028 of precipitation and water vapor in the tropics: 2. Physical interpretation of the amount effect, *J. Geophys. Res.*,  
1029 113, 2008JD009943, <https://doi.org/10.1029/2008JD009943>, 2008.
- 1030 Risi, C., Bony, S., Vimeux, F., and Jouzel, J.: Water-stable isotopes in the LMDZ4 general circulation model:  
1031 Model evaluation for present-day and past climates and applications to climatic interpretations of tropical  
1032 isotopic records, *J. Geophys. Res. Atmos.*, 115, <https://doi.org/10.1029/2009JD013255>, 2010.
- 1033 Risi, C., Galewsky, J., Reverdin, G., and Briant, F.: Controls on the water vapor isotopic composition near the  
1034 surface of tropical oceans and role of boundary layer mixing processes, *Atmos. Chem. Phys.*, 19, 12235–12260,  
1035 <https://doi.org/10.5194/acp-19-12235-2019>, 2019.
- 1036  
1037 Risi, C., Muller, C., and Blossey, P.: Rain evaporation, snow melt, and entrainment at the heart of water vapor  
1038 isotopic variations in the tropical troposphere, According to Large-Eddy Simulations and a Two-Column Model,  
1039 *J. Adv. Model Earth Syst.*, 13, e2020MS002381, <https://doi.org/10.1029/2020MS002381>, 2021.
- 1040 Risi, C., Muller, C., Vimeux, F., Blossey, P., Vèdeau, G., Dufaux, C., and Abramian, S.: What controls the  
1041 mesoscale variations in water isotopic composition within tropical cyclones and squall lines? Cloud resolving  
1042 model simulations in radiative-convective equilibrium, *J. Adv. Model Earth Syst.*, 15, e2022MS003331,  
1043 <https://doi.org/10.1029/2022MS003331>, 2023.
- 1044 Ryu, S., Song, J. J., and Lee, G. W.: Radar–rain gauge merging for high-spatiotemporal-resolution rainfall  
1045 estimation using radial basis function interpolation, *Remote Sens.*, 17(3), 530;  
1046 <https://doi.org/10.3390/rs17030530>, 2025.
- 1047  
1048 Salamalikis, V., Argiriou, A. A., and Dotsika, E.: Isotopic modeling of the sub-cloud evaporation effect in  
1049 precipitation, *Sci. Total Environ.*, 544, 1059–1072, <https://doi.org/10.1016/j.scitotenv.2015.11.072>, 2016.

- 1050 Sapucci, L. F., Machado, L. A. T., Da Silveira, R. B., Fisch, G., and Monico, J. F. G.: analysis of relative  
 1051 humidity sensors at the WMO Radiosonde Intercomparison Experiment in Brazil, *J. Atmos. Oceanic Technol.*,  
 1052 22(6), 664–678, <https://doi.org/10.1175/JTECH1754.1>, 2005.
- 1053
- 1054 Saranya, P., Krishan, G., Rao, M. S., Kumar, S., and Kumar, B.: Controls on water vapor isotopes over Roorkee,  
 1055 India: Impact of convective activities and depression systems, *J. Hydrol.*, 557, 679–687,  
 1056 <https://doi.org/10.1016/j.jhydrol.2017.12.061>, 2018.
- 1057 Sarkar, M., Bailey, A., Blossey, P., de Szoeki, S. P., Noone, D., Quiñones Meléndez, E., Leandro, M. D., and  
 1058 Chuang, P. Y.: Sub-cloud rain evaporation in the North Atlantic winter trade winds derived by pairing isotopic  
 1059 data with a bin-resolved microphysical model, *Atmos. Chem. Phys.*, 23, 12671–12690,  
 1060 <https://doi.org/10.5194/acp-23-12671-2023>, 2023.
- 1061
- 1062 Sengupta, S., Bhattacharya, S. K., Parekh, A., Nimya, S. S., Yoshimura, K., and Sarkar, A.: Signatures of  
 1063 monsoon intra-seasonal oscillation and stratiform process in rain isotope variability in northern Bay of Bengal  
 1064 and their simulation by isotope enabled general circulation model, *Clim. Dynam.*, 55, 1649–1663,  
 1065 <https://doi.org/10.1007/s00382-020-05344-w>, 2020.
- 1066 Sengupta, S., Bhattacharya, S. K., Sunil, N. S., and Sonar, S.: Quantifying raindrop evaporation deficit in  
 1067 general circulation models from observed and model rain isotope ratios on the west coast of India, *Atmosphere*,  
 1068 14, 1147, <https://doi.org/10.3390/atmos14071147>, 2023.
- 1069 Sinha, N., and Chakraborty, S.: Isotopic interaction and source moisture control on the isotopic composition of  
 1070 rainfall over the Bay of Bengal, *Atmos. Res.*, 235, 104760, <https://doi.org/10.1016/j.atmosres.2019.104760>,  
 1071 2020.
- 1072 Stewart, M. K.: Stable isotope fractionation due to evaporation and isotopic exchange of falling waterdrops:  
 1073 Applications to atmospheric processes and evaporation of lakes, *J. Geophys. Res.*, 80, 1133–1146,  
 1074 <https://doi.org/10.1029/JC080i009p01133>, 1975.
- 1075 Tao, W., Chen, J., Li, Z., Wang, C., and Zhang, C.: Impact of aerosols on convective clouds and precipitation,  
 1076 *Rev. Geophys.*, 50, 2011RG000369, <https://doi.org/10.1029/2011RG000369>, 2012.
- 1077 Trenberth, K. E.: Atmospheric moisture recycling: role of advection and local evaporation, *J. Climate*, 12,  
 1078 1368–1381, [https://doi.org/10.1175/1520-0442\(1999\)012<1368:AMRROA>2.0.CO;2](https://doi.org/10.1175/1520-0442(1999)012<1368:AMRROA>2.0.CO;2), 1999.
- 1079 Utsav, B., Deshpande, S. M., Das, S. K., and Pandithurai, G.: Statistical characteristics of convective clouds  
 1080 over the Western Ghats derived from weather radar observations, *J. Geophys. Res.-Atmos.*, 122,  
 1081 <https://doi.org/10.1002/2016JD026183>, 2017.
- 1082 Villiger, L., Dütsch, M., Bony, S., Lothon, M., Pfahl, S., Wernli, H., Brilouet, P.-E., Chazette, P., Coutris, P.,  
 1083 Delanoë, J., Flamant, C., Schwarzenboeck, A., Werner, M., and Aemisegger, F.: Water isotopic characterization  
 1084 of the cloud–circulation coupling in the North Atlantic trades – Part 1: A process-oriented evaluation of  
 1085 COSMOiso simulations with EUREC4A observations, *Atmos. Chem. Phys.*, 23, 14643–14672,  
 1086 <https://doi.org/10.5194/acp-23-14643-2023>, 2023.
- 1087
- 1088 Vimeux, F., Tremoy, G., Risi, C., and Gallaire, R.: A strong control of the South American SeeSaw on the intra-  
 1089 seasonal variability of the isotopic composition of precipitation in the Bolivian Andes, *Earth and Planet. Sci.*  
 1090 *Lett.*, 307, 47–58, <https://doi.org/10.1016/j.epsl.2011.04.031>, 2011.
- 1091 Wang, B., Ding, Y., and Sikka, D.: Synoptic systems and weather, *The Asian Monsoon*, 131–201, 2006.
- 1092 Wang, R., Gentine, P., Yin, J., Chen, L., Chen, J., and Li, L.: Long-term relative decline in evapotranspiration  
 1093 with increasing runoff on fractional land surfaces, *Hydrol. Earth Syst. Sci.*, 25, 3805–3818,  
 1094 <https://doi.org/10.5194/hess-25-3805-2021>, 2021.
- 1095 Wang, S., Zhang, M., Che, Y., Chen, F., and Qiang, F.: Contribution of recycled moisture to precipitation in  
 1096 oases of arid central Asia: A stable isotope approach, *Water Resour. Res.*, 52, 3246–3257,  
 1097 <https://doi.org/10.1002/2015WR018135>, 2016.

- 1098 Worden, J., Noone, D., Bowman, K. et al.: Importance of rain evaporation and continental convection in the  
1099 tropical water cycle, *Nature*, 445, 528–532, <https://doi.org/10.1038/nature05508>, 2007.
- 1100 Worden, J., Noone, D., Galewsky, J., Bailey, A., Bowman, K., Brown, D., Hurley, J., Kulawik, S., Lee, J., and  
1101 Strong, M.: Estimate of bias in Aura TES HDO/H<sub>2</sub>O profiles from comparison of TES and in situ HDO/H<sub>2</sub>O  
1102 measurements at the Mauna Loa observatory, *Atmos. Chem. Phys.*, 11, 4491–4503, <https://doi.org/10.5194/acp-11-4491-2011>, 2011.
- 1104 Wu, Y., Gao, J., Zhao, A., Niu, X., Liu, Y., Ratnasekera, D., Gamage, T. P., and Samantha, A. H. R.: One-year  
1105 continuous observations of near-surface atmospheric water vapor stable isotopes at Matara, Sri Lanka, reveal a  
1106 strong link to moisture sources and convective intensity, *Atmos. Chem. Phys.*, 25, 4013–4033,  
1107 <https://doi.org/10.5194/acp-25-4013-2025>, 2025.
- 1108  
1109 Xiao, F., Zhu, B., and Zhu, T.: Inconsistent urbanization effects on summer precipitation over the typical  
1110 climate regions in central and eastern China, *Theor. Appl. Climatol.*, 143, 73–85,  
1111 <https://doi.org/10.1007/s00704-020-03404-z>, 2021.
- 1112 Xing, M., Liu, W., Hu, J., and Wang, Z.: A set of methods to evaluate the below-cloud evaporation effect on  
1113 local precipitation isotopic composition: a case study for Xi'an, China, *Atmos. Chem. Phys.*, 23, 9123–9136,  
1114 <https://doi.org/10.5194/acp-23-9123-2023>, 2023.
- 1115  
1116 Xu, H., Guo, J., Tong, B., Zhang, J., Chen, T., Guo, X., Zhang, J., and Chen, W.: Characterizing the near-global  
1117 cloud vertical structures over land using high-resolution radiosonde measurements, *Atmos. Chem. Phys.*, 23,  
1118 15011–15038, <https://doi.org/10.5194/acp-23-15011-2023>, 2023.
- 1119 Yoshimura, K., Kanamitsu, M., Noone, D., and Oki, T.: Historical isotope simulation using reanalysis  
1120 atmospheric data, *J. Geophys. Res.*, 113, 2008JD010074, <https://doi.org/10.1029/2008JD010074>, 2008.
- 1121 Zaitchik, B. F., Macalady, A. K., Bonneau, L. R., and Smith, R. B.: Europe's 2003 heat wave: a satellite view of  
1122 impacts and land–atmosphere feedbacks, *Int. J. Climatol.*, 26, 743–769, <https://doi.org/10.1002/joc.1280>, 2006.
- 1123 Zhang, F., Huang, T., Man, W., Hu, H., Long, Y., Li, Z., and Pang, Z.: Contribution of recycled moisture to  
1124 precipitation: A modified d-excess based model, *Geophys. Res. Lett.*, 48, e2021GL095909,  
1125 <https://doi.org/10.1029/2021GL095909>, 2021.
- 1126 Zhu, G., Zhang, Z., Guo, H., Zhang, Y., Yong, L., Wan, Q., Sun, Z., and Ma, H.: Below-cloud evaporation of  
1127 precipitation isotopes over mountains, Oases, and Deserts in Arid Areas, *J. Hydrometeorol.*, 22, 2533–2545,  
1128 <https://doi.org/10.1175/JHM-D-2>  
1129  
1130  
1131  
1132